Uncut chip geometry determination for cutting forces prediction in orthogonal turn-milling operations considering the tool profile and eccentricity

Harry Otalora-Ortega[a,*], Patxi Aristimuño Osoro[a], Pedro Arrazola Arriola[a]

[a] *Mondragon Unibertsitatea, Faculty of Engineering, Mechanical and Manufacturing Department, Loramendi 4; 20500 Arrasate-Mondragon*

Abstract

The cutting forces generated in machining are responsible for the tool deflection, part distortion, and features as chatter; therefore, their accurate estimation is fundamental to defining stable and safe working conditions to increase workpiece accuracy and productivity. Turn-milling is a conventional milling operation while the workpiece is simultaneously rotating. These operations enable manufacturing pieces with bosses or eccentricities; particularly, in large-sized industries such as aeronautics, naval power, and nuclear energy. Despite its wide use, relatively few studies are available regarding cutting forces and their implication in the process. Then, the effects of some cutting parameters over the process are not well detailed, for example, the tool profile and eccentricity. The numerical model presented in this research covers the cases of tool eccentricity and tool profile, such as torus and spherical end mills in orthogonal turn-milling operations. The model accurately determines the uncut chip geometry, validated theoretically against a CAD representation of the chip with errors below 3%. Furthermore, a set of milling trials was proposed to compare the chip mass and the cutting forces estimated by the model with those measured from the trials in torus and spherical profiles. The experimental validation results correlate in both tests presenting in the case of the mass errors below 3.5% and the cutting-forces errors around 12%. The validated model allows exploring a wider scenario of simulations where the eccentricity and the tool profile are the studied variables. The main findings drawn from the experiments and simulations are that the tool profile and the eccentricity affect the material removal rate. Its wrong selection reduces the chip volume and leaves material where it is supposed to be removed; then, the geometrical errors force to reprocess the workpiece, negatively impacting manufacturing productivity.

Keywords: turn-milling, uncut chip geometry, cutting forces prediction, numerical geometrical model

Nomenclature

β	Feed angle
κ	Tangential angle of the edge
λ	Flute helix angle
$\overline{x_m}$	Material profile points position in x coordinate
$\overline{x_t}$	Tool profile points position in x coordinate
$\overline{y_m}$	Material profile points position in y coordinate
$\overline{y_t}$	Tool profile points position in y coordinate
$\overline{z_m}$	Material profile points position in z coordinate
$\overline{z_t}$	Tool profile points position in z coordinate
ϕ	Tool rotation angle
$\phi_{\lambda\{i,j\}}$	Phase angle of each point resulting from the helix angle

*Corresponding author: Tel.: +34 943 712 185; fax: +34 943 000 500

Email address: hyotalora@mondragon.edu (Harry Otalora-Ortega)

ϕ_{th} Angles between flutes with respect to the reference flute

θ Workpiece rotation angle

A Instantaneous chip area

a_p Depth of cut

$d\phi$ Differential of angle

$d\phi_i$ Differential of angle in the i^{th} position

dA Area of each element

$dF_a(\phi)$ Differential of force in the axial direction

$dF_r(\phi)$ Differential of force in the radial direction

$dF_t(\phi)$ Differential of force in the tangential direction

e Eccentricity

f_a Axial feed

f_t Tangential feed

$F_x(\phi)$ Total force signal in X coordinate

$F_y(\phi)$ Total force signal in Y coordinate

f_z Feed per tooth

$F_z(\phi)$ Total force signal in Z coordinate

f_{at} Axial feed per tooth

$F_{xphn}(\phi)$ Phased force signal in X coordinate of the n^{th} cutting edge

$F_{xrf}(\phi)$ Force in X coordinate referenced for a single edge pass

$F_{yphn}(\phi)$ Phased force signal in Y coordinate of the n^{th} cutting edge

$F_{yrf}(\phi)$ Force in Y coordinate referenced for a single edge pass

$F_{zphn}(\phi)$ Phased force signal in Z coordinate of the n^{th} cutting edge

$F_{zrf}(\phi)$ Force in Z coordinate referenced for a single edge pass

i Row counter

j Column counter

K_a Axial cutting Coefficient

K_r Radial cutting Coefficient

K_t Tangential cutting Coefficient

L Lag matrix to phase the whole uncut chip geometry

l_s Radial usable length of the egdge

n_t Tool rotational speed

n_w Workpiece rotational speed

O_t Tool origin

O_w Workpiece origin

P_{mi} Material profile in the i^{th} position

P_{ti} Tool profile in the i^{th} position

r_n Nose radius or Insert radius

r_t Tool radius

R_w Workpiece radius

Vc Cutting Speed

X X coordinate

X_t Tool x coordinate

X_w Workpiece x coordinate

Y Y coordinate

Y_t Tool y coordinate

Y_t+ Positive direction in the Y tool coordinate

Y_w Workpiece y coordinate

Z Z coordinate

z Number of cutting flutes

Z_t Tool z coordinate

Z_w Workpiece z coordinate

1. Introduction

Increments in machining productivity, more complex workpiece geometries, and demanding tolerances result from machine tools with combinations of the linear and rotational controlled axis [1, 2]. These versatile machines enable more complex movements between the workpiece and the cutting tool, including more parameters to consider in the optimum operating window. Cutting forces resulting from the machining process are significant for scientifically guiding the selection of machining parameters and tool geometries [3]; resulting in the need for more complete models that take into account tool profile and the workpiece geometry such as the 4 and 5 axis milling [4, 5, 6].

Simultaneously milling while the workpiece rotates is knows as turn-milling. This manufacturing approach presents some relevant advantages that highlight it as an alternative to conventional turning, especially with hard-to-cut materials [7]. These advantages are mainly: (i) Lower cutting force and temperatures due to the intermittent cutting compared with conventional turning; that gives the edge time to cool down during the not material-removing period [8, 9]. (ii) Consequently, the tool life presents considerable increments [7, 8]. (iii) Augmented versatility to manufacturing rotational shapes such as cylindroid or ellipsoids. Additionally, it allows the bosses manufacturing by milling operations on the rotational surfaces [10]. (iv) As the workpiece rotation feeds the process, the rotational speed is relatively low compared with the tool rotation speed; therefore, this technology is convenient to produce massive eccentric workpieces [11]. (v) Based on the low rotational speed of the workpiece, the centrifugal forces in this spindle are considerably lower than those in turning [12]. (vi) The lower cutting forces and the slow rotations may prevent undesired deformations of the workpiece during the manufacturing process [10, 13]. Especially benefiting thin-walled workpieces from the advantages previously described.

Despite the listed advantages, turn-milling operations do not comply with the traditional flat-end milling model [14]. This behavior corresponds to the additional variables that take place in turn-milling and modify the chip forming process [15]. For example, the uncut chip geometry presents considerable differences from that obtained by face milling, as some authors show in their publications. Crichigno [9] described an uncut chip geometry where the end edge presents a considerable portion of the uncut chip geometry. Yan et al. [16] presented an approach of orthogonal cutting force prediction and the effect of the variable depth of cut in the chatter in turn-milling operations. This complete work considers only the flank cutting zone. Then, Karaguzel et al. published a different uncut chip geometry from that found by Crichigno using the same modeling methodology [12]. This difference shows that the uncut chip geometry is very sensitive to the cutting parameters like the depth of cut (a_p) due to the workpiece curvature. Zhu et al. presented an analytical model to find the evolution of the chip thickness in the large depth of cut regimen while the edge is rotating for both the centric and eccentric cases [11]. The referenced Zhu et al. concluded that the eccentricity in turn-milling operations is a determining feature of the uncut chip geometry. It is the orthogonal distance of separation of the tool and workpiece axes. The centric case occurs when both axes intersect each other, while the rest of the scenarios are known as eccentric turn-milling, as explained by Zhu and Karaguzel et al. [11, 12]. Otalora-Ortega et al. presented an analytical approach finding the uncut chip geometry in both large and small depth of cut regimens; additionally, they modeled the condition to identify the operating regimen [17]. The referenced work shows the equations of the boundary lines from the uncut chip geometry based on the cutting parameters of the process. Plotting all the lines in the same domain is represented the evolution of the uncut chip geometry during the edge rotation with highly accurate results. The uncut chip was validated theoretically by CAD comparison, experimentally by cut chip weight measurement, and cutting force prediction. This work may have the most extensive experimental plan performing robust predictions of uncut chip geometry and cutting forces; however, all of the models from Crichigno to Otalora-Ortega are only valid with flat end mills.

Qiu et al. [18] presented an approach to predict cutting forces in orthogonal turn-milling with round inserts validated with an experimental plan of four different cutting conditions, but the eccentricity was not varied. Comak et al. [19] proposed an approach to predict cutting force and other variables of the machine tool as torque, power requirement from a model of generalized chip thickness distribution as a function of linear feed drive motions, tool, and workpiece spindle rotations validated with an experimental plan of one cutting condition with

a flat end mill. These works show how the augmented amount of parameters difficult the proper cutting parameter definition; not to mention their optimization to work in an acceptable operating window. Additionally, these developments work for a specific tool profile; then, they are not valid if the edge geometry is different [15].

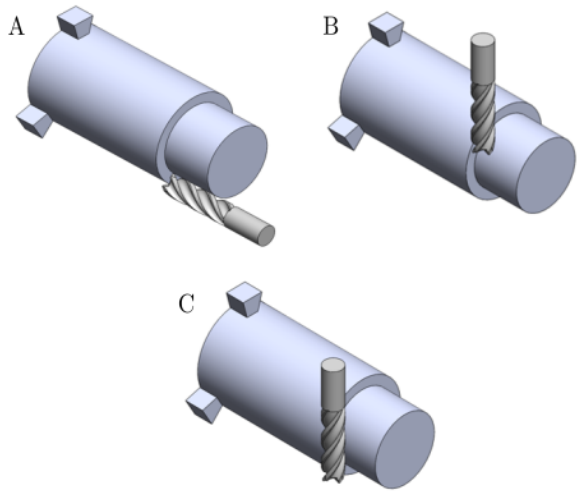

Figure 1: A: Coaxial turn-milling. B: Orthogonal turn-milling. C: Tangential turn-milling.

According to Karaguzel, the alignment between the workpiece and tool rotational axes is the feature to classify the turn-milling operations, as presented in figure 1 [12]. Schulz defined that the tool and workpiece only could be aligned coaxially or orthogonally [20]. On the one hand, the coaxial case has the workpiece and tool rotation axes aligned parallelly. On the other hand, the orthogonal case has those axes orthogonal, and they should intersect with each other. Schulz et al. found that machining in coaxial turn-milling results in an outstanding surface finishing, with roughness comparable with grinding, [21]. Savas et al. introduced the tangential turn-milling in the existent classification [22]. In this case, the flank of the mill performs the cut. The remarkable surface finishing result of turn-milling operation reduces the need to reprocess the workpiece later, thus shortening the production chain [23].

Literature states consistently that the cutting force depends on two factors: the behavior of the material during the cutting process and the uncut chip geometry evolution [24]. In this research, the specific force model represents the material behavior.

The tool profile effect has been apparently few studied but is an important feature to keep in mind to reach high material removal rate conditions. Adding the fact that, is not well understood the eccentricity effect in the uncut chip geometry, due to the lack of theoretical validation. The analysis of this behavior might be interesting to set this parameter towards productivity optimization and determine the acceptable operation window.

This paper presents a numerical methodology representing the uncut chip geometry taking into account the tool profile. It is valid to spherical and torus end mills and might work for other tool profiles. Based on the movements of the tool in the 3D space, resulting from the tool linear displacements and workpiece rotation the uncut chip geometry can be determined and theoretically validated with a CAD comparison. Additionally, the geometrical model is used to estimate the cutting forces and is validated experimentally. Simulation scenarios are proposed to determine the eccentricity and tool profile effect over the cutting forces and uncut chip geometry. This is to elucidate the effect of these variables within the machining process due to the complexity of the problem resulting of the augmented cutting parameters. The knowledge produced by this research might be useful to improve the machining performance without sacrificing the quality of the piece and increasing productivity.

2. Modeling the tool profile

The market offers a wide variety of tool profiles such as flat, torus, spherical, or barrel end mills. Additionally, there is a wide offer of indexable insert mills with diverse tool profiles. This feature determines the shape of the uncut chip geometry, mostly the inner and outer chip boundaries. For example, the uncut chip generated from a flat end mill is not the same as that got from a spherical nose mill, even with the same cutting conditions. Based on this, the tool profile shape is fundamental to predict the cutting forces accurately in any machining operation, and turn-milling is not the exception. With this in mind, it is essential to model the geometry of the tool in turn-milling.

Revolving the bi-dimensional profile of the tool results in the 3D mill geometry. If the $X - Z$ plane is selected to define the bi-dimensional profile, mathematical expressions can be stated to follow the profile geometry. These expressions could be

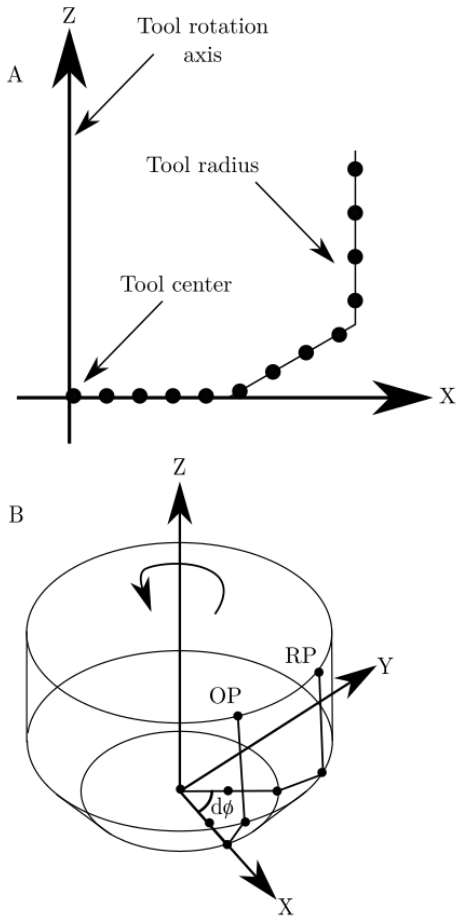

Figure 2: A: Arbitrary bi-dimensional tool profile. B: Rotated profile around the z axis (OP: Original profile. RP: Rotated profile).

even piecewise functions because all of the expressions have the same independent variable X. In this specific scenario, the volume of the mill is defined with the rotated profiles around the Z axis in a full turn. It is proposed that the main domain of the profile is saved in the $\overline{x_t}$ variating between zero to tool radius (r_t) and is going to be divided in differentials of radius set by the programmer as shown in equation 1. Depending on the profile functions, the z coordinate can be calculated point by point and saved in the $\overline{z_t}$ vector, as represented in equation 1. Based on the selection of the plane $X-Z$, the Y coordinate is zero, so these values are saved in the vector $\overline{y_t}$, see figure 2 A and B. With this information is possible to plot the points in a 3D coordinate system space, where the coordinates of each point (X, Y, Z) are the correspondent in the saved vectors $\overline{x_t}, \overline{y_t}, \overline{z_t}$. For example, the first point should have the following coordinates $(0, 0, f(0))$ and the last point $(r_t, 0, f(r_t))$ based on equation 1.

$$\begin{aligned} \overline{x_t} &= [0, x_1, x_2, x_3, ..., r_t] \\ \overline{y_t} &= [0, \quad 0, \quad 0, \quad 0, ..., 0] \\ \overline{z_t} &= [f(0), f(x_1), f(x_2), f(x_3), ..., f(r_t)] \end{aligned} \tag{1}$$

If these three vectors are concatenated in a matrix, it is possible to systematically rotate a differential of angle ($d\phi$) around the z axis as shown in equation 2. Notice the subindex i of the angle differential ($d\phi_i$) in the equation. This is because the revolution is expressed like a vector that starts in zero, augmenting in fixed steps until it reaches 2π; the number of steps will define the angular resolution of the mill. Each rotated profile must be saved to built-in the whole mill geometry as presented in figure 2 B. This geometry is compound by a set of points in the 3D Cartesian coordinate system.

$$P_{ti} = \begin{bmatrix} \cos(d\phi_i) & -\sin(d\phi_i) & 0 \\ \sin(d\phi_i) & \cos(d\phi_i) & 0 \\ 0 & 0 & 1 \end{bmatrix} [\overline{x_t}, \overline{y_t}, \overline{z_t}] \tag{2}$$

The tool profile might be complex, and it might not correspond exactly with the shape left in the material. This is due to the whole edge is not supposed to remove material. Indeed, it is expected that only the external segment of the edge performs the cut, as shown in figure 3. Therefore, it is necessary to define the material profile as explained previously, where the point positions are saved in the vectors shown in equation 3.

$$P_{mi} = \begin{bmatrix} \cos(d\phi_i) & -\sin(d\phi_i) & 0 \\ \sin(d\phi_i) & \cos(d\phi_i) & 0 \\ 0 & 0 & 1 \end{bmatrix} [\overline{x_m}, \overline{y_m}, \overline{z_m}] \tag{3}$$

Other important features of the mill, such as the amount of cutting edges and the helix angle, affect the uncut chip geometry strongly. However, these features are taken into account within the **Sections 3 & 4**.

3. Kinematics in turn-milling operations

The relative movements between the tool and workpiece are also determining in the chip formation process. The rotational movement of the workpiece changes the traditional kinematic variables in

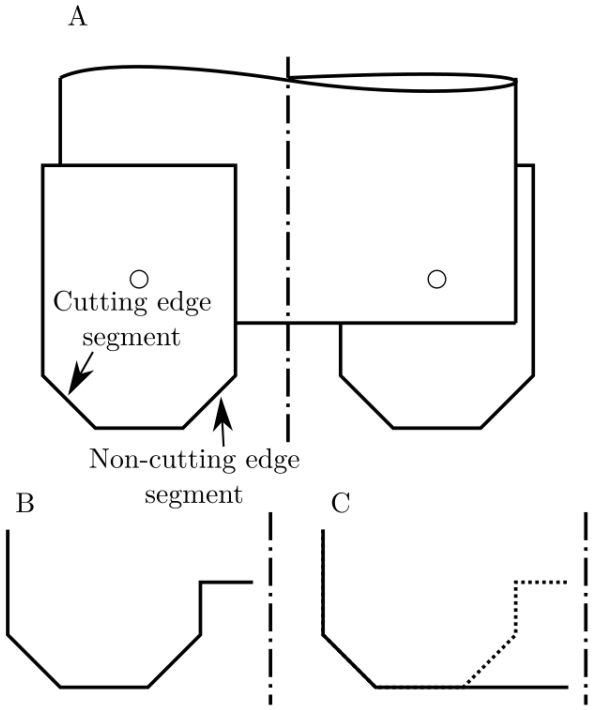

Figure 3: A:Indexable insert tool with arbitrary geometry. B: Tool profile to be rotated. C: Material profile obtained after the pass of the tool.

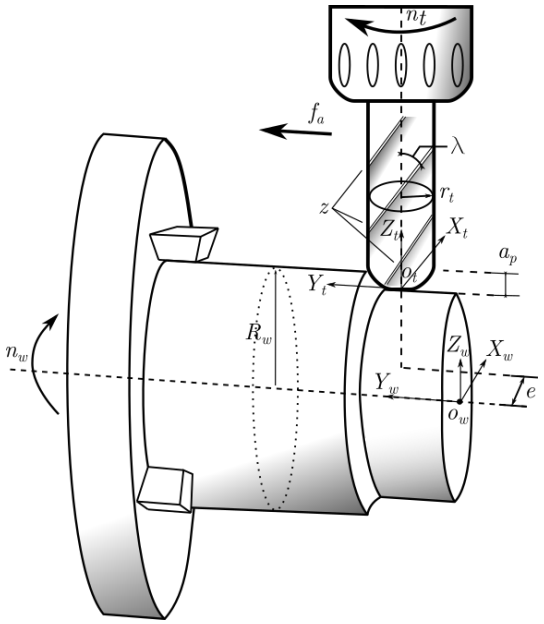

Figure 4: Orthogonal turn-milling kinematics. R_w Workpiece radius, n_w Workpiece rotational speed [rpm], r_t Tool radius [mm], n_t Tool rotational speed [rpm], f_a Axial feed [mm/Workpiece rev],a_p Depth of cut [mm], z Number of cutting edges, e Eccentricity [mm], λ Helix angle [^{o}], O_t Tool origin, X_t Tool x direction, Y_t Tool y direction, Z_t Tool z direction, O_w Workpiece origin, X_w Workpiece x direction, Y_w Workpiece y direction, Z_w Workpiece z direction.

milling. The workpiece is considered static while the tool performs the movements. Figure 4 shows the kinematic variables that take place in the orthogonal turn-milling process. The thicker arrows represent movements driven by the machine: workpiece rotational speed (n_w), tool rotational speed (n_t), and axial feed (f_a). Then, are the geometrical variables: workpiece radius (R_w), tool radius (r_t), number of cutting flutes (z), and helix angle of the tool (λ). The following are the operative parameters: depth of cut (a_p), and eccentricity (e). Hereinafter, the origins and directions of each one of them: workpiece origin (O_w) with its $X, Y, \& Z$ directions (X_w, Y_w, Z_w) and tool origin (O_t) with its correspondent linear directions (X_t, Y_t, Z_t) as presented in figure 4.

The tool and material profiles explained in the previous section were described from the tool origin. However, the turn-milling movements have to be seen from the workpiece coordinate framework due to the workpiece is also performing a rotation movement. Therefore, it is necessary to relate both origins of coordinates between each other, as shown in equation 4 and represented in figure 4. Therefore, it is possible to translate the material and tool profiles to the cutting position viewed from the workpiece coordinate system.

$$\begin{aligned} X_t &= X_w + e \\ Y_t &= Y_w \\ Z_t &= Z_w + (R_w - a_p) \end{aligned} \tag{4}$$

The approach followed in this research is to define the uncut chip geometry, projecting the material profile points considering the turn-milling movements in one tooth pass and comparing them with the tool profile. Therefore, the kinematic variables of the process are fundamental to set where were translated and rotated the material profile points to the previous tooth pass position. The cutting speed is simplified as the same as conventional milling; due to the slow rotation of the workpiece, this movement is negligible, as shown in equation 5.

$$Vc = \frac{2\pi r_t n_t}{1000} \tag{5}$$

The axial feed (f_a) movement is performed in the workpiece axial direction and is a parameter selected by the machine tool operator. This parameter indicates the distance covered by the tool in one workpiece revolution. However, to translate the tool points to the previous edge position, it is necessary to find the distance covered in the workpiece axial direction but per edge, not per workpiece revolution. Then, the axial feed per tooth (f_{at}) is a portion of the axial feed (f_a) as shows equation 6. As the tool moves in the axial direction, it also covers a perimeter distance called tangential feed (f_t) and exposed in equation 7. The workpiece angle rotation per edge (θ) is shown in equation 8. The axial and tangential feeds are orthogonal and simultaneous between each other. This condition results in a helical trajectory around the workpiece with a feed angle (β) found as shows in equation 9. The distance moved in the feed angle (β) direction is the feed per tooth (f_z) and is determined, as shown in equation 10. The variables previously explained are shown in figure 5. However, all the variables shown are not in scale due to they are usually tiny compared with the tool and workpiece dimensions.

$$f_{at} = \frac{f_a n_w}{n_t z} \tag{6}$$

$$f_t = 2\pi R_w \tag{7}$$

$$\theta = \frac{2\pi n_w}{n_t z} \tag{8}$$

$$\beta = \arctan\left(\frac{f_a}{f_t}\right) \tag{9}$$

$$f_z = \frac{n_w \sqrt{f_a^2 + f_t^2}}{n_t z} \tag{10}$$

The relative movements occurring during the turn-milling operation can be associated with the material and toolsets of points. This approach assumes that the linear transformations done to these sets are commutative in the workpiece origin. Additionally, it is supposed that the uncut chip geometry is the volume between the material profile and tool profile; hence the sets of points can represent these instants by linear transformations of the matrix of points coordinates. Note that the tool geometry on the workpiece origin is considered an instant after the edge has performed the cut. Consequently, the linear transformations performed to the material profile matrix will find the set of points that represents the material to be removed.

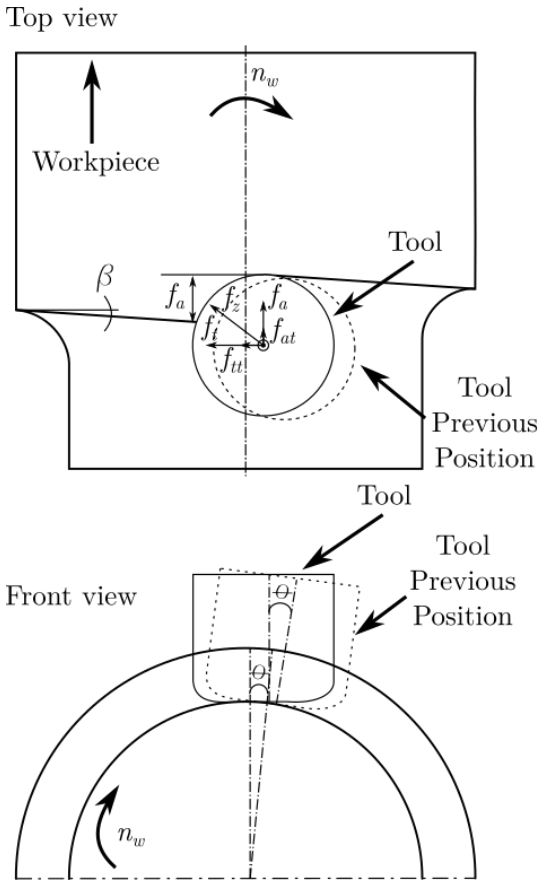

Figure 5: Feeds and angles in orthogonal turn-milling.

The workpiece rotation effect is represented as a rotation of the material set of points at a θ angle in the cutting position. Hence, the coordinate matrix in the workpiece origin is the dot product of the material set of points viewed from the workpiece origin with the rotation matrix around the Y_w axis as shows equation 11.

$$[X_m i, Y_m i, Z_m i] = \begin{bmatrix} \cos(\theta) & 0 & \sin(\theta) \\ 0 & 1 & 0 \\ -\sin(\theta) & 0 & \cos(\theta) \end{bmatrix} [X_{mw}, (Y_{mw} - f_{at}), Z_{mw}] \tag{11}$$

4. Determination of instantaneous chip geometry

Both sets of points are in the previous and after cut positions, but they do not represent the uncut chip geometry. Therefore, it is necessary to perform the point interpolation, the invalid point removal processes and include the tool helix angle effect.

4.1. Comparable point interpolation

The challenge is that the profiles are not comparable to find the chip thickness, although all of the points are in the right position. Figure 6 presents a tool profile scheme. In black, the tool profile in the $X-Z$ plane, notice the coordinate Y is zero. Additionally, it is represented as a rotation of this profile at a $d\phi$ angle, shown as the next black line. In solid gray, the material profiles are represented once the workpiece rotation and axial feed movements have been performed.

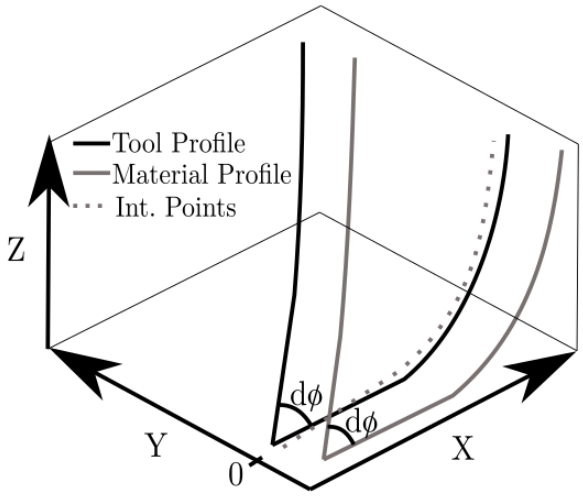

Figure 6: Diagram of some portion of the sets of points of the tool profile, material profile, and material interpolated profile.

Form the rotation and translation of the material profiles due to the process kinematics do not directly compare with the tool profile. However, the material profile contains the whole information to calculate the uncut chip geometry. For this reason, it is necessary to interpolate the points in the same plane of the correspondent profile in the "tool profile" position.

As can be inferred from the **section 2** the sets of points were described in a cylindric coordinate grid,

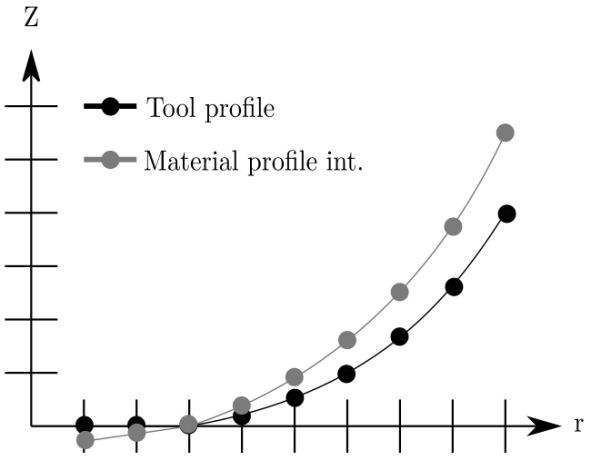

Figure 7: Tool profile in position and the material interpolated profile in the same plane.

since the geometry is described in terms of the radius (X coordinate), angle ($d\phi$), and height (Z coordinate). Therefore, if the polar grid (radius and angle) is used to interpolate the points based on the "material profile" set, it is possible to approximate the height of the points valid to establish the uncut chip geometry. These points are represented in figure 6 as the dotted gray line in the tool coordinate system.

The interpolated points share the radial domain of the "material profile interpolated" set. For this reason, the expectable results per each $d\phi$ are presented in figure 7. The interpolation reconstructs the whole geometry of the tool based on the radial and angular coordinates taken from the "tool profile" position. Hence, the interpolated points lie exactly in the same radial coordinate of the after cut position, but in a different height of Z.

4.2. Selection of feasible points

The feasible point selection is performed by taking into account the material removal zone, the workpiece curvature, and the axial feed effect. This is necessary because the point interpolation process recreated the whole tool geometry. However, the cutting process is performed only with a fraction of this geometry.

- Selection of points that represent material

It is important to notice that the "Material profile" position defines the boundary where the tool will find material to remove. Therefore, the space

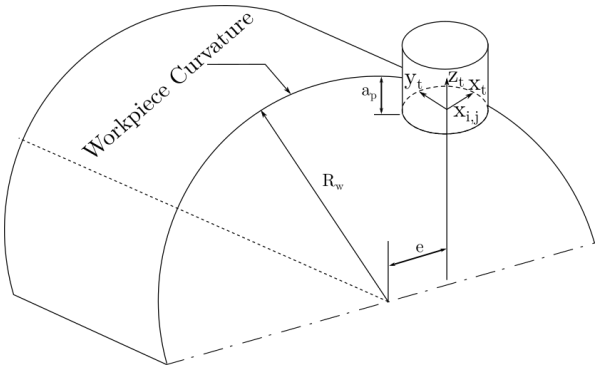

Figure 8: Variables in the workpiece curvature effect calculation.

below the material interpolated profile represents material to be removed, while the space over the tool profile has already been removed. Therefore, all of those points where the "tool profile" is greater than the "material profile" in the Z direction are neglected. This selective process is performed in both "material interpolated and tool" profiles.

- Effect of the workpiece curvature

Additionally, it is necessary to consider the effect of workpiece curvature. For this reason, all the points above of this curvature are discarded. The points are discriminated based on the following inequality presented in equation 12. The expression to the right represents the curvature seen from the tool origin of coordinates. The eccentricity (e) is the distance of separation of the workpiece and tool rotating axes, see figure 8.

$$Z_{i,j} > \sqrt{R_w^2 - (X_{i,j} + e)^2} - (Rw - ap) \qquad (12)$$

- Effect of the axial feed

The axial feed is a significant parameter to describe the uncut chip geometry, as have shown by Otalora-Ortega et al. and Zhu [17, 11]. The axial feed is the parameter that indicates how much distance is covered by the tool in the axial direction by each workpiece rotation. Then, as the tool describes a helical trajectory around the workpiece, the helix pitch corresponds to the axial feed parameter, as shown in figure 9. Here are presented the variables that define the point selection due to the axial feed f_a, and the axial feed angle β.

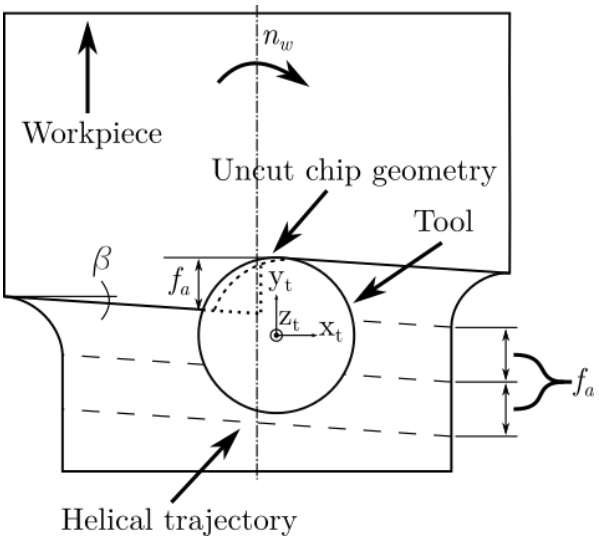

Figure 9: Effect of axial feed on the helical trajectory of the tool around the workpiece.

The axial feed is also related to the radial engagement of the tool, determining as well which portion of the mill performs the cut. Therefore, there is a physical boundary line where axis feed angle β is indicated in figure 9. In this way, the material to be removed is in the Y_t+ direction starting from this line. Therefore the uncut chip geometry is defined by this boundary. Then, all the points that fulfill the inequality presented in equation 13 should be removed.

$$Y_{i,j} \leq \tan(\beta) X_{i,j} + \left(\tan(\beta)\sqrt{rt^2 - (rt - fa)^2} + (rt - fa)\right) \qquad (13)$$

- Closing the uncut chip geometry

Neglecting points of the material and tool profile result in an open geometry with different shapes. It is necessary to add points to the material interpolated profile to close the uncut chip geometry. Figure 10 shows an arbitrary plane of the uncut chip geometry where the realistic points are represented as circles. The neglected points are represented with "x" markers, and the added points are represented with triangle markers. The added points are at the same height as the maximum valid point in the material interpolated profile.

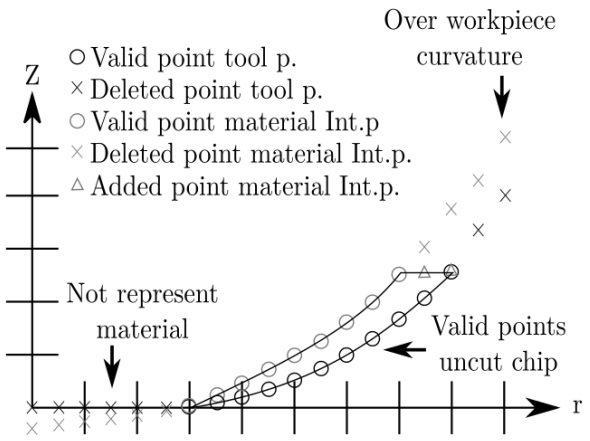

Figure 10: Point selection and addition to close the uncut chip geometry.

4.3. Effect of the tool helix angle

The tool helix angle (λ) has a strong effect on the cutting forces and the chip forming process. Figure 11 shows the helix angle in a flat end mill. This characteristic is also presented in exchangeable insert mills.

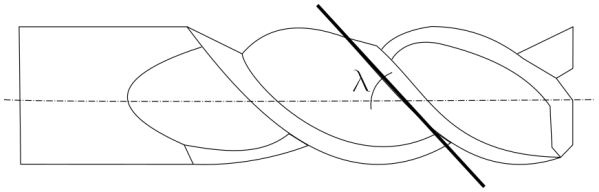

Figure 11: Tool helix angle in a flat end mill.

At first sight, the workpiece-tool intersection does not present any change due to the helix angle due to the tool kinematic is not related to this feature. However, it does present an effect on the chip formation process. The cutting edge is rotating around the tool axis; then, the edge tip performs approximately a circular movement during the cutting process, as shown in figure 12 in the left zone. Consequently, the material lies on the rake face following the tool helix angle λ. As a result, it is necessary to increase the tool rotation to compensate for the helix angle effect. It is easier to see if the process is unrolled, considering the edge moves linearly but not rotationally. A diagram of this scenario is presented in figure 12 on the right side. So, the edge tip covers an arc segment ($r_t\phi$), and the uncut chip geometry is deformed following the helix angle.

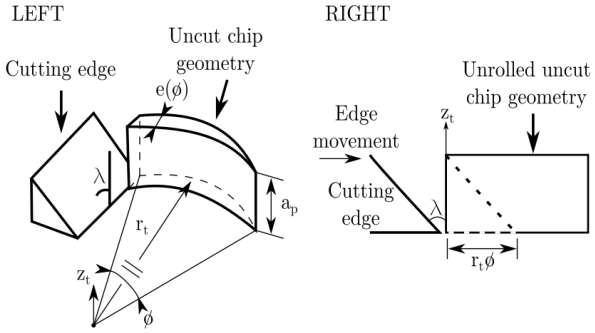

Figure 12: Chip formation process taking into account the helix angle. LEFT: Diagram of the chip forming process. RIGHT: Unrolling of the chip forming process

The geometry can be deformed, adding a phase angle to the points. This phase angle is found by a simple trigonometric expression, assuming the helix angle constant, equation 14 shows how to find the phase angle of each profile. Moreover, this phase angle depends on the (Z_t) direction due to the rest of the terms are simply constants, which means more height in the profile more phase angle. As the approach is numeric, it is necessary to discretize and introduce it to the points.

$$\phi_{\lambda\{i,j\}} = \frac{Z_{i,j}}{\tan(\lambda) r_t} \tag{14}$$

The discretization is done based on the differential of rotation angle $d\phi$ selected to perform the 2D profile rotation to recreate the tool geometry in the "after cut" position presented in **section 2**. Equation 15 shows how to determine the lag matrix L. Notice that the values of the matrix belong to the natural numbers. Consequently, they must be integer quotient of the fraction expressed in equation 15. This integer matrix shows the number of positions each point has to be phased in the ϕ direction.

$$L_{i,j} = \frac{\phi_{\lambda\{i,j\}} d\phi}{2\pi} : \{L_{i,j} \in \mathbb{Z}\} \tag{15}$$

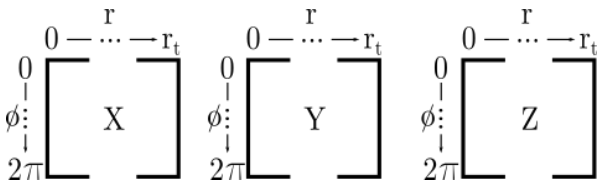

Figure 13: Data structure in the 3D coordinate system

The data have a cylindrical coordinate structure separated in the Cartesian coordinates (X, Y, Z) as

shown in figure 13. In other words, each matrix has the coordinates of the points in its corresponding Cartesian direction. However, the rows of each matrix are associated with the position in the tool radius and the columns to the angular (ϕ) position around the Z_t axis. This is convenient because the lag matrix L has the same dimension of the coordinates matrix (X, Y, Z). Consequently, it is possible to relate the number of cells that have to be displaced in the angular direction to deform the geometry. In graphical terms, the displacements of the cells in the angular direction (vertical) within the matrix (X, Y, Z) displace the points generating the effect sketched in figure 14.

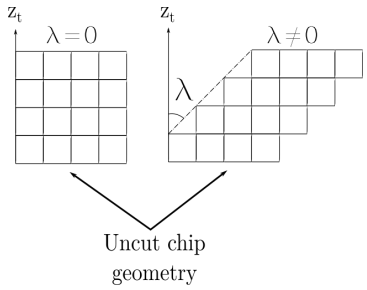

Figure 14: Effect of the helix angle λ over the modeled uncut chip geometry.

4.4. Model implementation in an arbitrary case

As a matter of example, the procedure explained previously is reproduced with the conditions presented in table 1. These cutting conditions are not necessarily realistic. They were selected to amplify the workpiece rotations and axial feed to exaggerate the uncut chip geometry and have noticeable graphical results. The idea is to perform simulations through this model with workshop cutting conditions as presented in **section 7** and **section 8**. The radial discretization counts with 100 divisions and the angular with 72 divisions.

The geometry to be analyzed is the torus mill with a nose radius of $r_n = 6mm$ as presented in table 1. Then, the bi-dimensional tool and materials profiles in the $(X - Z)$ plane are described by the piecewise functions presented in equation 16.

Table 1: Arbitrary cutting conditions to recreate the uncut chip geometry

Parameter	Symbol	Value	Units
Cutting speed	V_c	297	m/min
Tool radius	r_t	12.5	mm
Tool rot speed	n_t	3782	rpm
Nose Radius	r_n	6	mm
Workpiece radius	R_w	95	mm
Workpiece rot Speed	n_w	30	rpm
Axial feed	f_a	15	$\frac{mm}{w_{orkpiece}rev}$
Depth of cut	a_p	2	mm
Eccentricity	e	4	mm
Cutting edges	z	2	-
Helix Angle	λ	85	^{o}

$$Z_t(x) = \begin{cases} rn & : 0 \leq x \leq (r_t - r_n) \\ - & \sqrt{r_n^2 - (x - (r_t - r_n))^2} + r_n \\ & : (r_t - 2r_n) < x \leq r_t \end{cases}$$
$$Z_m(x) = \begin{cases} 0 & : 0 \leq x \leq (r_t - r_n) \\ - & \sqrt{r_n^2 - (x - (r_t - r_n))^2} + r_n \\ & : (r_t - r_n) < x \leq r_t \end{cases} \quad (16)$$

Figure 15 (a) shows the resulting profiles in the $(X-Z)$ space, where the Y coordinate is zero for all the points. The profile covers heights from zero to 6 mm. Then, These profiles are rotated around the Z axis, as shown in figure 15 (b). After this operation, the tool and material profiles are fully described; however, it is necessary to translate them to the cutting position viewed from the workpiece origin. Notice the effect of the eccentricity in the center of the geometry changes from $(0, 0, 0)$ to $(4, 0, 93)$ in figure 15 (c). Additionally, the workpiece radius effect occurs, modifying the Z axis variating from 93 to 99.

With the geometry in this position, it is possible to include the workpiece rotation and the axial feed translation. Figure 15 (d) shows a front view of both tool (orange) and material (blue) profiles. Although these surfaces cut each other, forming the uncut chip geometry, it is impossible to compare them directly. Figure 15 (e) illustrates the situation. As the geometry has been displaced and rotated, the resulting material profile (continuous green line) can not be compared with the tool profile (continuous blue line). Therefore, the interpolation of the material geometry is performed, gen-

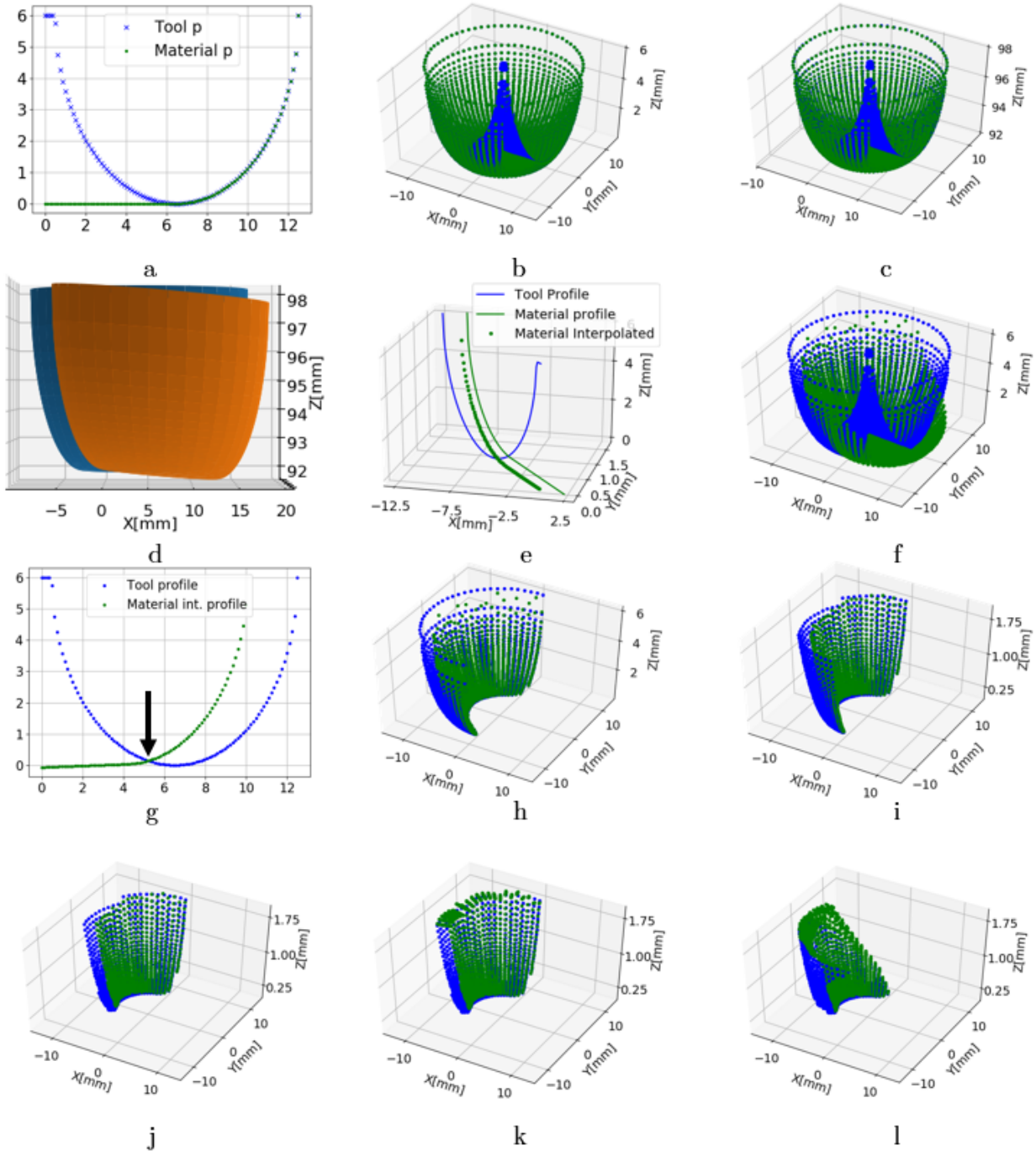

Figure 15: a: 2D tool profile in $X-Z$. b: Tool geometry generated by the 2D rotation around the Z axis. c: Tool geometry in the workpiece coordinate system O_w. d: Previous cut surface (Orange). After cut surface (blue). e: Random tool profile. After cut (Blue). Previous cut (Green). Interpolated profile (Dotted green). f: After cut tool geometry (blue). Previous cut interpolated geometry (green). g: Random tool profile to remove the unrealistic points. h: Points considered material to remove. i: Effect of the workpiece curvature. j: Effect of the axial feed. k: Uncut chip geometry with augmented angular resolution. l: effect of the helix angle over the uncut chip geometry.

erating an approximation of the profile suitable to carry out the profile comparison (dotted green line). This interpolation is executed to the whole tool geometry, generating the comparable scenario shown in figure 15 (f).

It is carried out to select feasible points to create the uncut chip geometry due to now. There are two comparable geometries. As explained in **subsection 4.2** each profile is compared to the material interpolated with tool profiles, and all of these points where the material interpolated profile has less height than the tool profile are neglected as shows figure 15 (g). In this figure, the arrow indicates the limit where the geometry starts to be realistic; then, all of the points to the left of this arrow are discarded. As a result of this operation, the geometry is reduced to that presented in figure 15 (h). It is then necessary to remove all of the points over the workpiece curvature as presented in figure 15 (i). Notice that the Z axis values change from 6 to 1.75 mm effect of the workpiece curvature and the eccentricity. The last point selection is performed to introduce the axial feed effect. Figure 15 (j) shows the point selection result. Notice the remaining geometry is a portion of that presented in figure 15 (i).

It is now necessary to close the profiles by adding the points representing the workpiece cylindrical surface. Therefore, figure 15 (k) shows green points in the top of the uncut chip geometry closing the profiles. The last manipulation to the geometry performed is the lag associated with the helix angle. Considering the big value of the helix angle, the uncut chip geometry is deformed as presented in figure 15 (l). As described in **subsection 4.3**, the phase or lag increases proportionally with the height of the point in the Z direction.

5. Theoretical validation of the uncut chip geometry

The numerical model presented until now needs to be checked to verify if it is accurately predicting the uncut chip geometry. Then, the predicted geometry is compared with the geometry obtained by CAD means reproducing the tool geometry and movements in the 3D space. As the comparison object is another representation of the uncut chip geometry, it is considered as a theoretical validation; in other words, to compare the uncut chip geometry obtained by two different methods. Comparing the evolution of the uncut chip area obtained by numerical means and CAD varying the cutting conditions. Hence, four simulation scenarios were proposed (T1, T2, T3, T4) with arbitrary cutting conditions, as shown in table 2. The main reasons to perform this test are: (i) It is necessary to ensure that the movements performed by the tool correspond to the linear transformations performed to the set of points proposed by this approach. (ii) The direct visual comparison does not represent the differences in display scale from Python and SolidWorks, as shown in figure 16. Hereinafter, the radial and angular discretization count with 1000 and 720 points, respectively.

Table 2: Cutting conditions of four validation scenarios (T1-T4). V_c: Cutting speed.r_t: Tool radius. n_t: Tool rot. speed. R_w: Workpiece radius. n_w: Workpiece rot. speed. f_a: Axial feed. a_p: Depth of cut. e: Eccentricity. z: Qty. of cutting edges. r_n: Nose radius.

Parameter	T1	T2	T3	T4
V_c [m/min]	400	200	300	100
r_t [mm]	10	15	8	12
n_t [rpm]	6366	2122	5968	1326
R_w [rpm]	45	45	45	45
n_w [mm]	12	8	8	15
f_a [mm/wrv]	12	9	3	15
a_p [mm]	2	1	1.5	2
e [mm]	3	1	5	2
z [-]	2	1	1	1
r_n [mm]	4	8	2	12

The instantaneous area calculation is based on the profiles that form the uncut chip geometry. This geometry is formed by the set of valid profiles, as explained in **section 4**. Therefore, each valid pair of profiles (tool & material Int.) generate the instantaneous area. As the tool and material profiles have the same amount of points, it is possible to build quadrilateral elements. The area of each element is found through the Gauss area formula, due each angular profile presents the ordered pair from the points in the radius and height direction (R, Z), see equation 17. It is important to order the element points clockwise to obtain positive magnitudes. Additionally, the first point should be repeated to close the polygon. The addition of all area differentials in the same cutting plane corresponds to the instantaneous area at some determined angle of rotation of the tool.

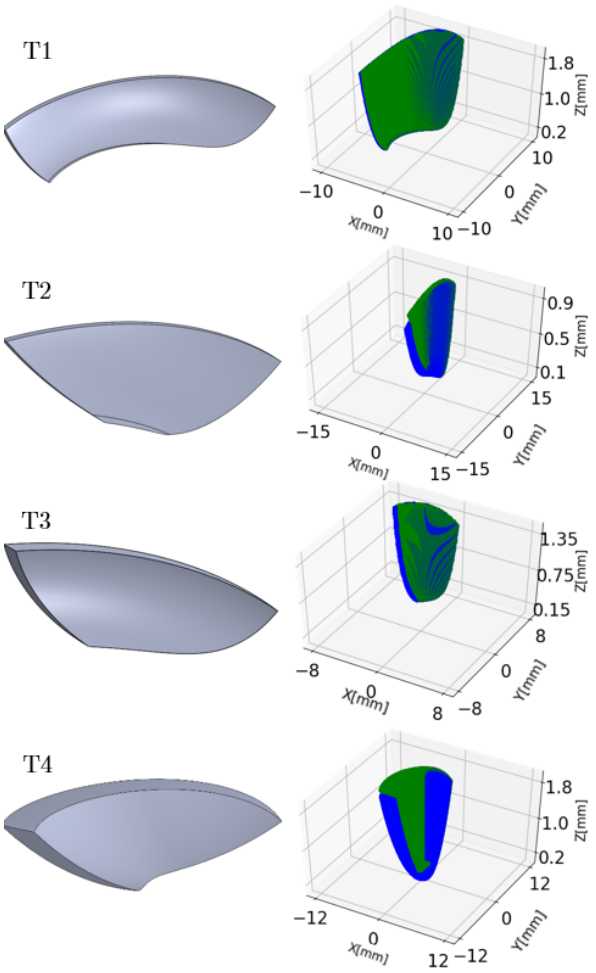

Figure 16: Graphical comparison of the CAD representation versus the results obtained from the numerical approach with the same cutting conditions presented in table 2.

$$dA = \frac{1}{2}|\sum_{i=1}^{n-1} R_i Z_{i+1} + R_n Z_1 - \sum_{i=1}^{n-1} R_{i+1} Z_i + R_1 Z_n| \tag{17}$$

Figure 17 shows the behavior of the instantaneous area. For example, the CAD representation of T4 is presented in figure 16. From left to right, it is easy to see how the chip area increases rapidly until it reaches the maximum and eventually drops. Besides, a great portion of the domain is zero, which means that the edge is not cutting material in this rotation portion. This behavior is presented in all the test and shows the evolution of the instantaneous area. It is important to remark that the chip thickness is not constant in the Z direction, and

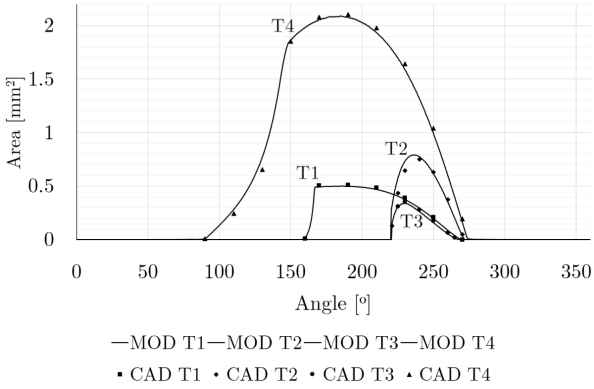

Figure 17: Comparison of instantaneous chip area evolution from the numerical approach vs the CAD.

the uncut chip geometry follows the workpiece curvature. Therefore, the instantaneous area evolution is the parameter for comparing approaches. The results are in good agreement presenting errors below 3%. These minor discrepancies might be associated with the simplifications assumed in the model.

6. Cutting forces prediction

The determination of the uncut chip geometry is fundamental for the cutting force prediction due to this geometry determines the magnitude and direction of the forces. As the geometrical model discretizes the geometry in finite elements, it is possible to determine the force differential of each element. Those differentials were estimated using the specific force model. This approach considers that the cutting forces are proportional to the instantaneous area removed by the edge during the rotation. It is important to remark that the differentials of force found by this approach are in the cutting, feed, and penetration directions. These directions are three-dimensional and orthogonal, but they do not necessarily coincide with the dynamometer coordinate sensor. Indeed, the cutting, feed, and penetration directions are deeply related to the edge geometry reported by Otalora-Ortega et al. [17].

6.1. Cutting forces

Consider a round insert tool in an arbitrary position removing material, as shown in figure 18. It is possible to see the front and side views of the tool performing the cut. Detail A shows how this instantaneous chip geometry is discretized in finite elements and aligned the differential of force with the

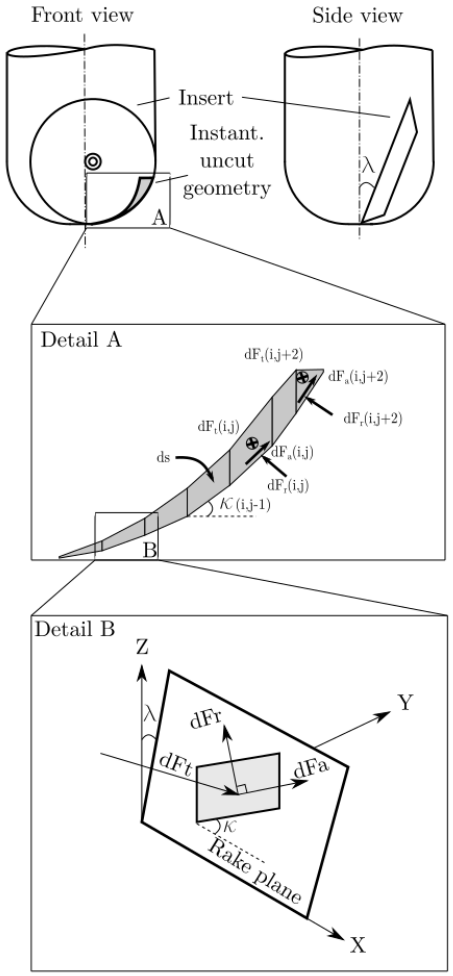

Figure 18: Differential of force per element and geometrical parameters for cutting force prediction

edge shape. Additionally, detail A shows the uncut chip normal to the rake plane of the mill. However, this plane is not necessarily aligned with the dynamometer coordinate system. In this scheme is rotated the helix angle (λ). Zooming in one finite element, detail B shows the rake plane, the force differentials, and the tangential angle of the edge (κ) concerning the plane ($X-Y$) from the uncut chip geometry and the force differentials. Note that the cutting direction is normal to the rake plane, inclined the helix angle (λ). Then, there are the feed and penetration directions that are co-planar and orthogonal, completing the orthogonal base described in equation 18. The feed direction is perpendicular to the edge instead of the penetration, parallel to the edge. Then, by determining the tangential angle of the edge (κ), the state of force in-plane can be determined.

$$\begin{aligned} dF_t(\phi) &= K_t dA(\phi, r) \\ dF_r(\phi) &= K_r dA(\phi, r) \\ dF_a(\phi) &= K_a dA(\phi, r) \end{aligned} \tag{18}$$

Equation 18 determines the general state of the forces of each element; however, it is not practical because the element directions are changing with the edge shape and helix angle as presented in figure 18. Therefore, it is necessary to change the coordinates system from the elements to the dynamometer reference. This is done by projecting the general state of the forces of each element in the dynamometer reference system and summing the components of force, as shown in equation 19. Note that the differential of force has a subindex *rf, which means reference edge, see figure 19.

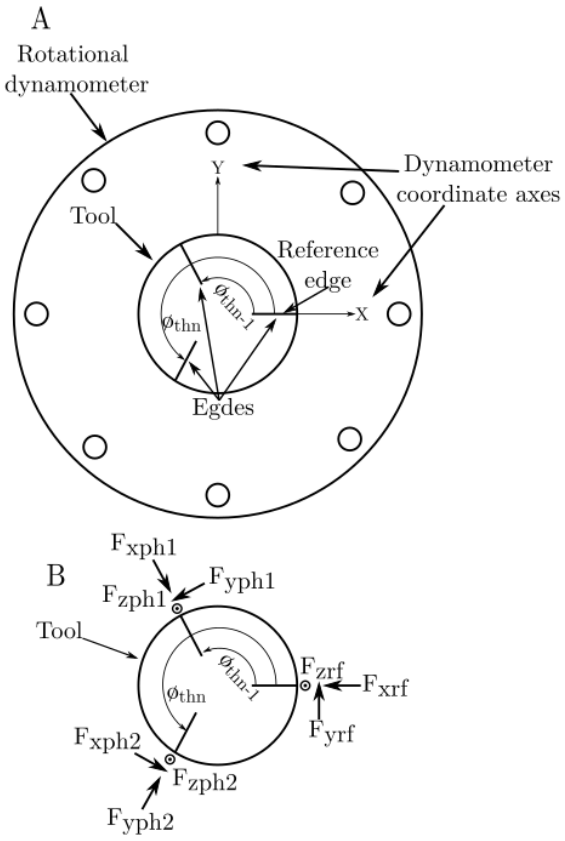

Figure 19: A: Suggested set up Tool-dynamometer. B: Tool general state of force.

$$\begin{bmatrix} dF_{xrf}(\phi) \\ dF_{yrf}(\phi) \\ dF_{zrf}(\phi) \end{bmatrix} = \begin{bmatrix} 0 & -\sin(\kappa(i,j) & \cos(\kappa(i,j)) \\ \cos(\lambda) & \cos(\kappa(i,j))\sin(\lambda) & \sin(\kappa(i,j))\sin(\lambda) \\ -\sin(\lambda) & \cos(\kappa(i,j))\cos(\lambda) & \sin(\kappa(i,j))\cos(\lambda) \end{bmatrix} \begin{bmatrix} dF_t(\phi) \\ dF_r(\phi) \\ dF_a(\phi) \end{bmatrix} \tag{19}$$

The reference edge is that one that is aligned with the X coordinate in the radial direction and the Y coordinate in the tangential direction of the mill. This important clarification defines the whole state of the forces of the mill. Equation 19 allows to predict the magnitude of force of each element in the X (dF_x), Y (dF_y) and Z direction (dF_z). It is required to integrate the forces in the radial direction as shows equation 20. This integration is the force exerted by the material on edge as long as one revolution.

$$\begin{aligned} F_{xrf}(\phi) &= \int_0^r dF_x(\phi)dr \\ F_{yrf}(\phi) &= \int_0^r dF_y(\phi)dr \\ F_{zrf}(\phi) &= \int_0^r dF_z(\phi)dr \end{aligned} \tag{20}$$

These results also regard the scenario where the cutting edge is aligned with the X-axis of the rotational dynamometer, also called the reference edge. Then, to determine the cutting force of the rest of the edges is necessary to phase the reference forces $(F_{xrf}(\phi), F_{yrf}(\phi), F_{zrf}(\phi))$. For this reason, the phase process is based on the angle between the reference edge and each of the rest of the edges (ϕ_{th}). This phasing consists of rotating the uncut chip geometry around the Z_t axis the angle ϕ_{th} and project the cutting forces over the tool coordinate system as shown in equation 21. This process is performed as many as cutting edges have the tool.

$$\begin{bmatrix} F_x(\phi) \\ F_y(\phi) \\ F_z(\phi) \end{bmatrix} = \begin{bmatrix} F_{xrf}(\phi) \\ F_{yrf}(\phi) \\ F_{zrf}(\phi) \end{bmatrix} + \begin{bmatrix} \cos(\phi_{th}) & \cos(\phi_{th}) & 0 \\ \sin(\phi_{th}) & \sin(\phi_{th}) & 0 \\ 0 & 0 & 1 \end{bmatrix} \begin{bmatrix} F_{xrf}(\phi) & ... & F_{xphn}(\phi) \\ F_{yrf}(\phi) & ... & F_{yphn}(\phi) \\ F_{zrf}(\phi) & ... & F_{zphn}(\phi) \end{bmatrix} \tag{21}$$

As a matter of example, consider an end mill with 3 flutes, see figure 19 A. One of the flute radial edges must be aligned with the X coordinate of the rotational dynamometer. **Sections 2 to 4** allow finding the uncut chip geometry per flute. Equations 18 to 20 estimate the behavior of the force in the 3D direction during the tool revolution but only of the reference edge. These force estimations are the reference signals $(F_{xfr}, F_{yfr}, F_{zfr})$ and depend on the tool rotation. Then, these same signals but phased the angle ϕ_{thn} by equation 21 results in the tool general state of force as show figure 19 B.

6.2. Specific force coefficients determination methodology

The previous paragraphs have described detailed how to find the general force state of the tool within a revolution. Therefore, the only detail remaining to complete the force prediction is determining the specific force coefficients, based on the mechanistic methodology [8]. In general terms, it is considered that the force is proportional to the instantaneous area [8, 14]. The specific force is the ratio between the force and the instantaneous area. Based on this, face milling characterization trials determine the behavior of the tool-material set. In these trials, the feed per tooth (f_z) is the independent variable, and the forces in the dynamometer coordinate system are the dependent variable.

Consider to rewrite equation 21 as presented in equation 22. Additionally, in groove milling at the maximum area instant, the area differential corresponds to that shown in equation 23. Replacing dA from equation 23 in equation 22 results in equation 24. Reorganizing the terms is built equation 25. Based on the assumption that the equation 23 is valid in the maximum chip thickness of the mill rotation in a groove operation, integrating the force differentials is equal to the maximum cutting forces measured from experimental trials. The integration range is related to the κ angle. The grooving case

$$
\begin{aligned}
dF_x &= K_t 0 - K_r \sin(\kappa) dA + K_a \cos(\kappa) dA \\
dF_y &= K_t \cos(\lambda) dA + K_r \sin(\lambda)\cos(\kappa) dA + K_a \sin(\lambda)\sin(\kappa) dA \\
dF_z &= -K_t \sin(\lambda) dA + K_r \cos(\lambda)\cos(\kappa) dA + K_a \cos(\lambda)\sin(\kappa) dA
\end{aligned} \tag{22}
$$

$$
dA = f_z r_n \sin(\kappa) d\kappa \tag{23}
$$

$$
\begin{aligned}
dF_x &= -K_r \sin(\kappa)(f_z r_n \sin(\kappa) d\kappa) + K_a \cos(\kappa)(f_z r_n \sin(\kappa) d\kappa) \\
dF_y &= K_t \cos(\lambda)(f_z r_n \sin(\kappa) d\kappa) + K_r \sin(\lambda)\cos(\kappa)(f_z r_n \sin(\kappa) d\kappa) + K_a \sin(\lambda)\sin(\kappa)(f_z r_n \sin(\kappa) d\kappa) \\
dF_z &= -K_t \sin(\lambda)(f_z r_n \sin(\kappa) d\kappa) + K_r \cos(\lambda)\cos(\kappa)(f_z r_n \sin(\kappa) d\kappa) + K_a \cos(\lambda)\sin(\kappa)(f_z r_n \sin(\kappa) d\kappa)
\end{aligned} \tag{24}
$$

$$
\begin{aligned}
dF_x &= -K_r f_z r_n (\sin^2(\kappa) d\kappa) + K_a f_z r_n (\cos(\kappa)\sin(\kappa) d\kappa) \\
dF_y &= K_t f_z r_n \cos(\lambda)(\sin(\kappa) d\kappa) + K_r f_z r_n (\sin(\lambda)\sin(\kappa)\cos(\kappa) d\kappa) + K_a f_z r_n (\sin(\lambda)\sin^2(\kappa) d\kappa) \\
dF_z &= -K_t f_z r_n \sin(\lambda)(\sin(\kappa) d\kappa) + K_r f_z r_n (\cos(\lambda)\cos(\kappa)\sin(\kappa) d\kappa) + K_a f_z r_n (\cos(\lambda)\sin^2(\kappa) d\kappa)
\end{aligned} \tag{25}
$$

$$
\begin{aligned}
Fx &= \int dF_x = -\int_0^{\kappa_m} K_r f_z r_n (\sin^2(\kappa) d\kappa) + \int_0^{\kappa_m} K_a f_z r_n (\cos(\kappa)\sin(\kappa) d\kappa) \\
Fy &= \int dF_y = \int_0^{\kappa_m} K_t f_z r_n \cos(\lambda)(\sin(\kappa) d\kappa) + \int_0^{\kappa_m} K_r f_z r_n (\sin(\lambda)\sin(\kappa)\cos(\kappa) d\kappa) + \int_0^{\kappa_m} K_a f_z r_n (\sin(\lambda)\sin^2(\kappa) d\kappa) \\
Fz &= \int dF_z = \int_0^{\kappa_m} -K_t f_z r_n \sin(\lambda)(\sin(\kappa) d\kappa) + \int_0^{\kappa_m} K_r f_z r_n (\cos(\lambda)\cos(\kappa)\sin(\kappa) d\kappa) + \int_0^{\kappa_m} K_a f_z r_n (\cos(\lambda)\sin^2(\kappa) d\kappa)
\end{aligned} \tag{26}
$$

$$
\begin{aligned}
F_x &= -K_r f_z r_n \left(\frac{k_m}{2} - \frac{\sin(2\kappa_m)}{4}\right) + K_a f_z r_n \left(\frac{\sin^2(k_m)}{2}\right) \\
F_y &= K_t f_z r_n \cos(\lambda)(1 - \cos(\kappa_m)) + K_r f_z r_n \sin(\lambda) \left(\frac{\sin^2(k_m)}{2}\right) + K_a f_z r_n \sin(\lambda) \left(\frac{k_m}{2} - \frac{\sin(2\kappa_m)}{4}\right) \\
F_z &= -K_t f_z r_n \sin(\lambda)(1 - \cos(\kappa_m)) + K_r f_z r_n \cos(\lambda) \left(\frac{\sin^2(k_m)}{2}\right) + K_a f_z r_n \cos(\lambda) \left(\frac{k_m}{2} - \frac{\sin(2\kappa_m)}{4}\right)
\end{aligned} \tag{27}
$$

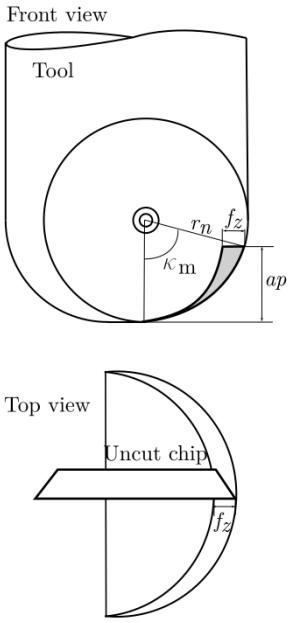

Figure 20: Maximum force instant in grooving for specific force coefficients determination.

starts in zero and finishes in κ_m, which is the maximum value of inclination presented by the uncut chip geometry (see figure 20). The result of the integration evaluated in the defined range is presented in equation 27; this set of equations determines a linear system in which the only unknown variables are the specific force coefficients. As a result of solving this linear system, finding the cutting coefficients for a specific trial is possible.

6.3. Specific force coefficients estimation

With a set of trials incrementing the feed per tooth, it is possible to determine the cutting coefficients in terms of the mean chip thickness. This is to generalize the cutting force prediction model presented in equation 21. The characterization trials were conducted in a vertical mill. The cutting tools selected to machine the aluminum 6063T5 samples consisted of a Sandvik exchangeable insert mill R300-15T08-07L with the helix angle ($\lambda = 0^o$) and round inserts R300-0724E-PM 1130 with nose radius ($r_n = 3.5$) mm for the torus profile. In the case of the spherical profile, an R216-16t08 indexable insert mill with the helix angle ($\lambda = -10^o$) and R216-16 03 E-M 1025 inserts with nose radius ($r_n = 8$) mm. The forces were captured by a Kistler rotational dynamometer 9123. Face milling trials were performed at cutting speed ($V_c = 400$ [m/s]), depth of cut ($a_p = 2$ [mm]) full width of cut ($a_e = 15$ and $a_e = 16$ [mm]) and feed per tooth ($f_z = [0.025, 0.05, 0.1, 0.175, 0.2]$ [mm/tooth]) and the peak of the force was taken after filter the signal with a low pass, cutoff 500 Hz, and order 2 to attenuate the sensor dynamic response; resulting in table 3. Three repetitions of each trial were carried out to ensure statistical representativeness.

Table 3: Cutting forces characterization trials

f_z $[mm]$	F_{xmax} $[N]$	F_{ymax} $[N]$	F_{zmax} $[N]$
Torus Mill			
0.025	-58.44	87.73	73.67
0.05	-85.64	134.03	103.53
0.1	-121.44	207.63	147.04
0.15	-144.65	244.40	171.69
0.2	-160.55	296.92	189.78
Spherical Mill			
0.025	-169.92	267.33	271.91
0.05	-235.39	394.52	371.38
0.1	-346.66	600.73	547.41
0.15	-432.61	778.53	694.15
0.2	-469.59	887.14	771.92

Torus mill

$$
\begin{aligned}
K_a &= 3.36(t(r,\phi))^{-0.822}) \left[\frac{N}{mm^2}\right] \\
K_t &= 199.69(t(r,\phi)^{-0.526}) \left[\frac{N}{mm^2}\right] \\
K_r &= 286.94(t(r,\phi)^{-0.418}) \left[\frac{N}{mm^2}\right]
\end{aligned}
\tag{28}
$$

Spherical mill

$$
\begin{aligned}
K_a &= -104.20(t(r,\phi))^{-0.482}) \left[\frac{N}{mm^2}\right] \\
K_t &= 830.71(t(r,\phi)^{-0.423}) \left[\frac{N}{mm^2}\right] \\
K_r &= 518.19(t(r,\phi)^{-0.498}) \left[\frac{N}{mm^2}\right]
\end{aligned}
$$

With the insert profile, it is possible to reproduce the uncut chip geometry during the grooving at the point of maximum force. Solving the equation system presented in equation 27 for each trial is possible to find the value of the ordinate showed in figure 21 and the abscissa values are the mean chip thickness of each trial. The most important feature is that this dataset is adjusted to power

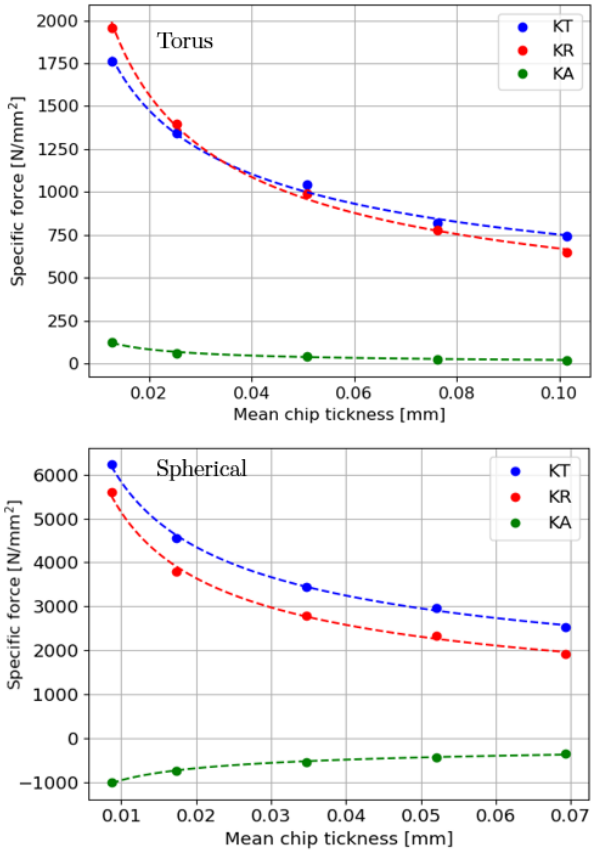

Figure 21: Specific Force coefficient in the cutting, feed and penetration directions. Up: Torus mill. Down: Spherical mill.

functions that have only the chip thickness as the independent variable; which means that using these expressions and inserting the chip thickness of each element is possible to find the magnitude of the specific force coefficient as shows equation 28.

7. Experimental validation of the model

The model to estimate the cutting forces has been completely defined in previous sections. Therefore, it requires experimental validation, consisting of running a set of cutting trials. Varying some cutting conditions and then comparing the resulting chip weight and cutting forces with the predictions obtained by this research model.

7.1. Methodology

Additionally to the machine tool, cutting tools, inserts, and material detailed in the previous section, the experimental setup counted with a rotary table to hold the workpiece as shown in figure 22. Consequently, the cutting conditions presented in table 4 are proposed to validate the model developed. These conditions were selected to evidence: (i) change in the uncut chip geometry, and (ii) the effect of the eccentricity in orthogonal turn-milling. It was intended not to exceed the suggestions of chip load given by the tool manufacturer.

Table 4: Experimental parameters for model validation

Rw [mm]		rt [mm]	z [-]	a_p [mm]	V_c $[\frac{m}{min}]$
44		7.5	1	2	400
		Torus Mill			
Tag	f_z $[\frac{mm}{th}]$	e [mm]	f_a $[\frac{mm}{W_p rev}]$	n_w [rpm]	MRR $[\frac{cm^3}{min}]$
fa3.5fz0.1e2	0.1	2	3.5	3	5.94
fa3.5fz0.1e4	0.1	4	3.5	3	5.94
fa3.5fz0.1e6	0.1	6	3.5	3	5.94
fa3.5fz0.2e2	0.2	2	3.5	6	11.88
fa3.5fz0.2e4	0.2	4	3.5	6	11.88
fa3.5fz0.2e6	0.2	6	3.5	6	11.88
fa12fz0.2e4	0.2	4	12	6	40.74
fa9fz0.2e6	0.2	6	9	6	30.56
		Spherical Mill			
fa8fz0.1e2	0.1	2	8	3	13.5
fa8fz0.1e4	0.1	4	8	3	13.5
fa8fz0.1e6	0.1	6	8	3	13.5
fa8fz0.2e2	0.2	2	8	6	27
fa8fz0.2e4	0.2	4	8	6	27
fa8fz0.2e6	0.2	6	8	6	27

It is important to remark that the geometrical model was used to keep the selected cutting conditions under safe values and the tool manufacturer recommendations. The experiment tried to show the effect of varying the chip geometry with two levels of feed per tooth (f_z) and three levels of axial feed (f_a). Additionally, the eccentricity values selected were lower, in the "optimum eccentricity" value ($e = r_t - l_s$), and greater of this value as reported by Karaguzel et al. [25]. The axial feed (f_a) levels selected are looking for producing a cylindrical surface.

7.2. Results and discussion

The chip mass results are shown in figure 23. The mass presents a thigh fitting between the theoretical value obtained through the model. The mean error is close to 3.5%; the small discrepancies may be related to the mass loss of the collected chips for their impact on the surroundings during the cutting process. The effect of increasing eccentricity is

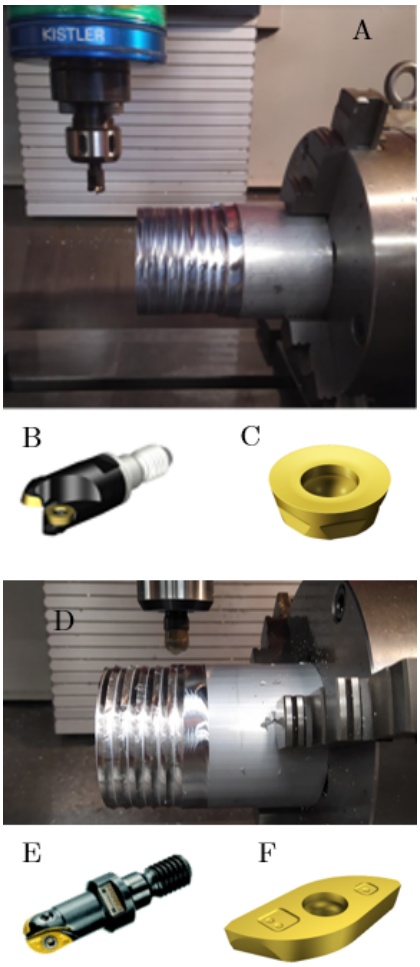

Figure 22: A. Experimental setup for torus mill. B: Indexable mill R300-15T08-07L. C: Insert R300-0724E-PM 1125. D: Experimental setup for spherical mill. E: Indexable mill 216-16T08. F: R216-16 03 E-M 1025

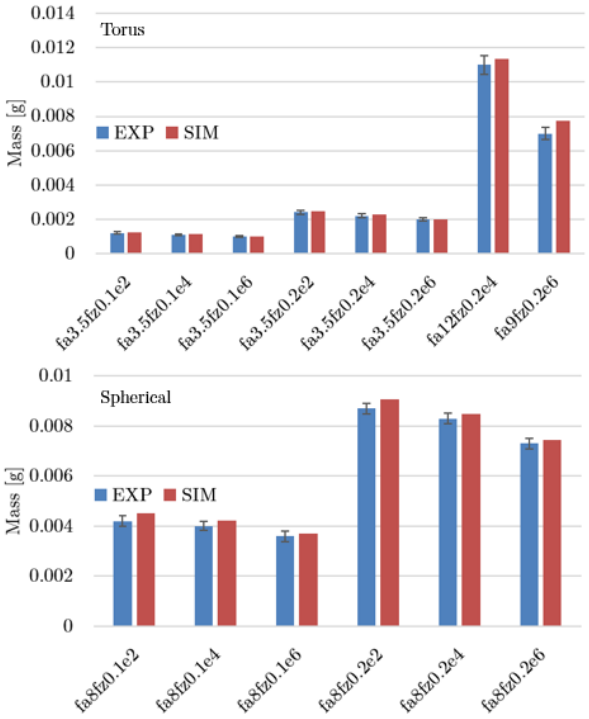

Figure 23: Cut chip mass compared with uncut chip mass. Up: Tours mill chip mass. Down: Spherical mill chip mass.

a slight decrease in the overall chip mass, suggesting that the eccentricity does affect the material removal rate. The presented mass changes support the idea that the eccentricity modifies the uncut chip geometry. Although the differences are small, the effect of eccentricity should not be discarded because, in larger diameter mills, the mass change might be more pronounced.

Additionally, the feed per tooth (f_z) response agreed with the expectation. An augment of the double of the mass could be appreciated in both simulation and experimental data. Interestingly, the decrement of mass resulting from the eccentricity is presented in both feed per tooth levels ($f_z = 0.1\&0.2\ mm/th$) . The effect of the axial feed for the torus mill (f_a) behaved as expected by the model, increasing considerably with the increment of this parameter, strongly affecting the material removal rate (MRR).

From the cutting conditions proposed in the experimental plan shown in table 4, the typical force signals obtained are similar to those shown in figure 24. The cutting force presents a dynamic and repetitive behavior as expected; this is due to the intermittent cutting proper from milling operations. The maximum peak frequency coincides with the tool rotational speed. The raw signal's dynamic response is strongly influenced by the dynamic parameters of the rotational dynamometer in the $(X - Y)$ plane. For this reason, it is recommended to pass a butter low pass filter with 500 Hz of cutoff frequency and order 2 to mitigate the dynamic response of the sensor.

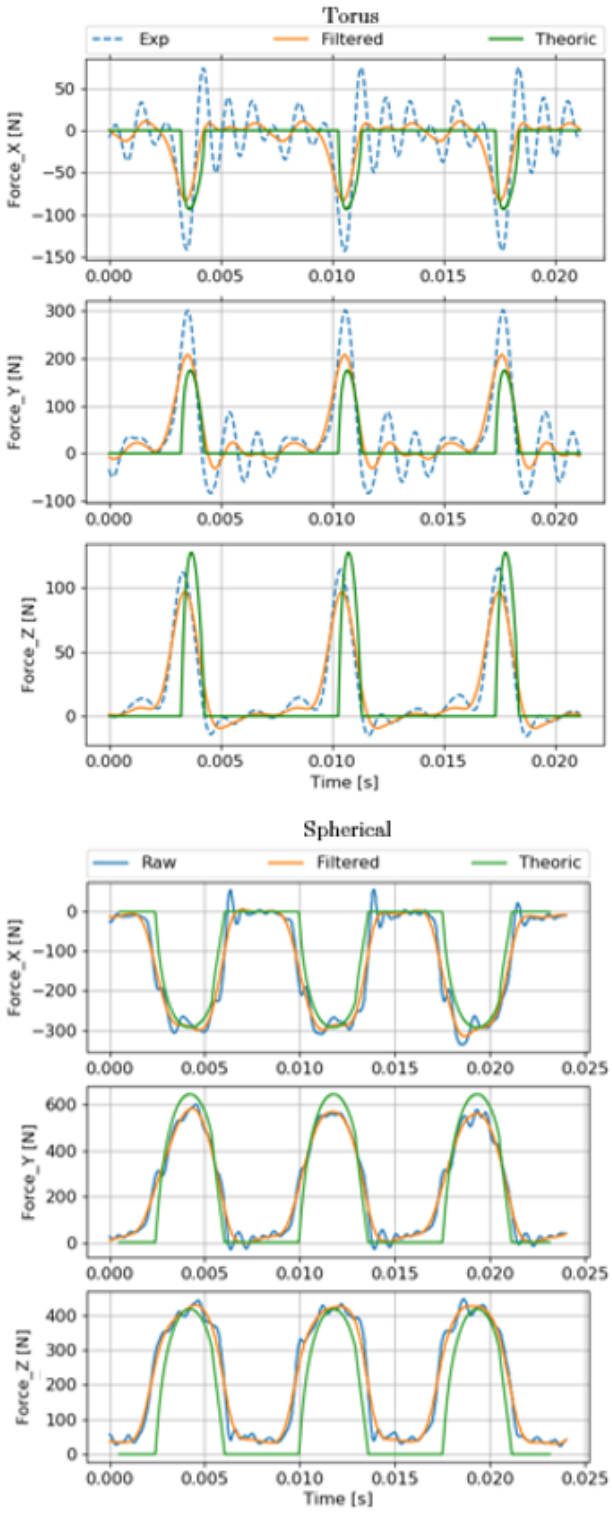

Figure 24: Up: Torus mill cutting forces in the time domain for the condition f_a : 3.5, f_z : 0.2, e : 2. Down: Spherical mill cutting forces in the time domain for the condition f_a : 8, f_z : 0.1, e : 2.

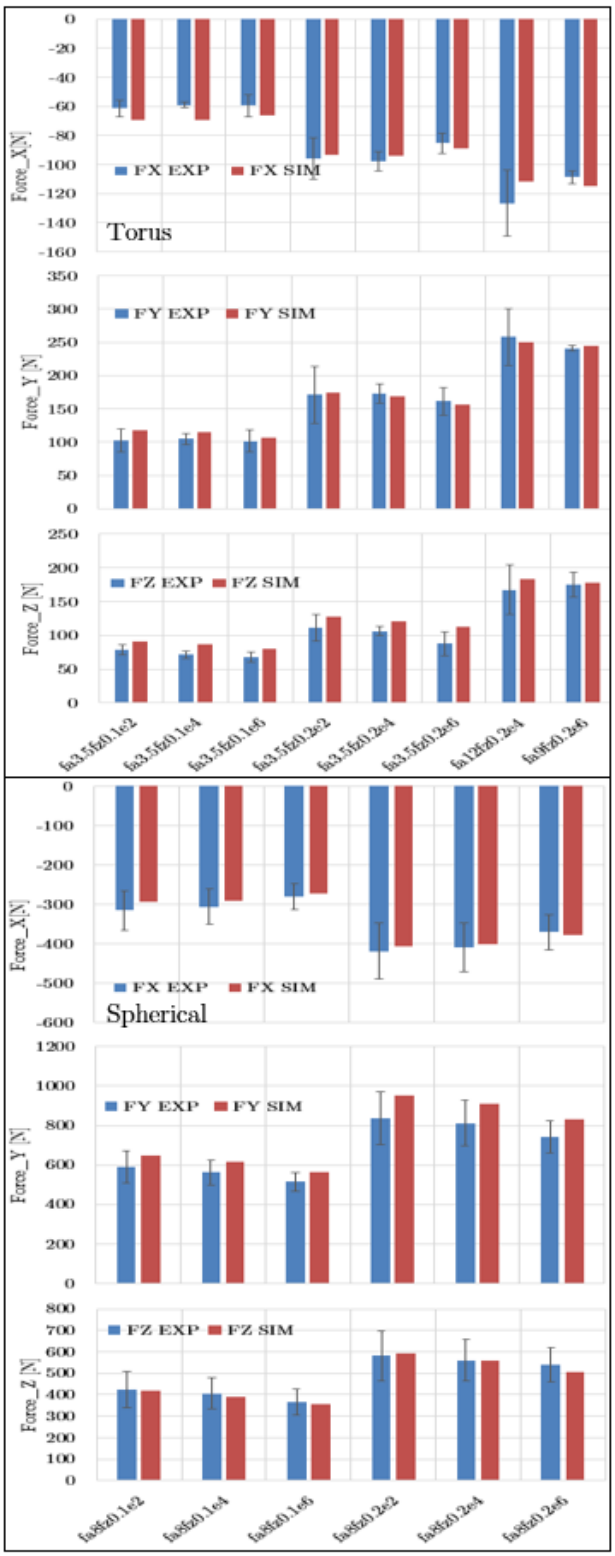

Figure 25: Maximum cutting force comparison in the whole experimental plan. Up: Torus mill results. Down: Spherical mill result.

The intermittent cutting presents an oscillating behavior where the force signal is proportional to the area during the cut and is zero when the edge has exceeded the exit angle completing the rotation. The cutting forces influence the workpiece deformation, the surface integrity, and the tool wear; thus, it is important to compare the maximum peak of the signal to validate the model and compare the cutting strategies. Therefore, figure 25 shows the complete experimental plan comparison. The cutting forces show a slight decrease when the eccentricity is augmented. This behavior correlates with the mass results, explaining the force reduction. The feed per tooth (f_z) has presented increments in the force as expected. Additionally, the model accurately determines the behavior of the forces when the axial feed is augmented. In general terms, the simulations fit tightly with the experimental data presenting errors around 12% for all the measurement axis (X, Y, Z). The mass variation concerning the eccentricity evidence that this parameter slightly modifies the material removal rate (MRR).

Additionally to the presented trials, uncut chip geometry simulations of experimental trials presented by Qiu et al. [18] are performed. The cutting conditions used in that research are presented in table 5. The material used was M300 steel. A 16 mm diameter indexable insert cutter was used and equipped with inserts of radius 4 mm. Qiu et al. also presented the cutting coefficients for this material presented in table 6. The geometry simulated was then used to obtain the forces by the methodology explained by Qui et al. [18]. Because the cutting coefficients methodology presented by Qui disagree with that explained in **sub-section 6.2**.

Table 5: Experimental cutting conditions performed by Qiu et al. [18].

Test No.	R_w [mm]	n_w [rpm]	n_t [rpm]	a_p [mm]	fv $[\frac{mm}{min}]$	e [mm]	z [-]
T1	49.5	2	1000	1.5	8	4	2
T2	48	2	2000	1	6	4	2
T3	48	4	2000	1	12	4	2
T4	43.5	2	2000	1.5	8	4	1

The typical results obtained by these simulations in the rotation angle domain is presented in figure 26 as presented by Qiu et al. in their publication. The simulated data exposed by Qiu was extracted from the published paper using the tool "WebPlotlDigitalizer" [26]. The magnitude and the frequency of the signals behave as expected. The complete comparison of the magnitude of cutting forces in the whole experimental plan defined by Qiu et al. presented in table 5.

Table 6: Cutting Coefficients reported by Qiu et al [18]

	K_tc $[\frac{N}{mm^2}]$	K_rc $[\frac{N}{mm^2}]$	K_te $[\frac{N}{mm}]$	K_re $[\frac{N}{mm}]$
Value	1929.95	1233.36	74.06	62.01

The simulation results agreed mutually, presenting small errors below 5% between the approaches. The differences in the modeling approaches might explain the small discrepancies. This behavior supports this research thesis and applies to a wider range of tool geometries and eccentricity values.

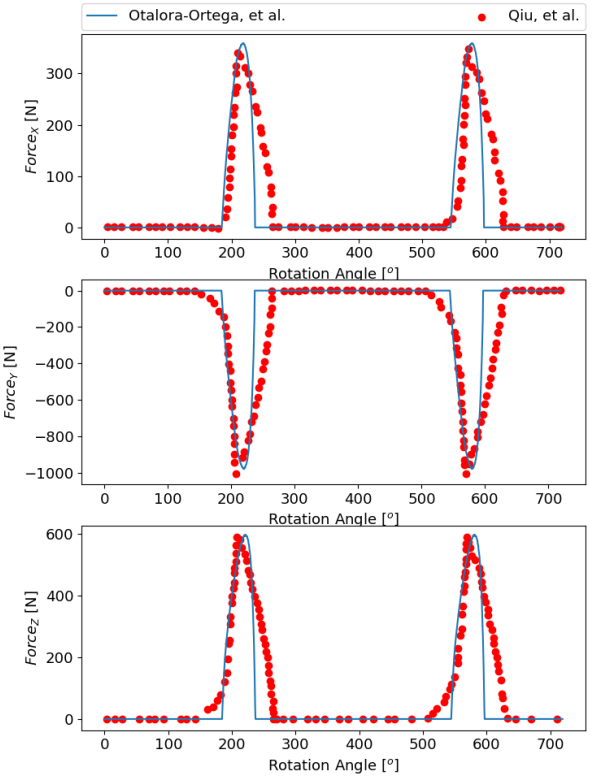

Figure 26: Trial 4 cutting forces reported from Qiu et al. [18] and simulated by the presented approach.

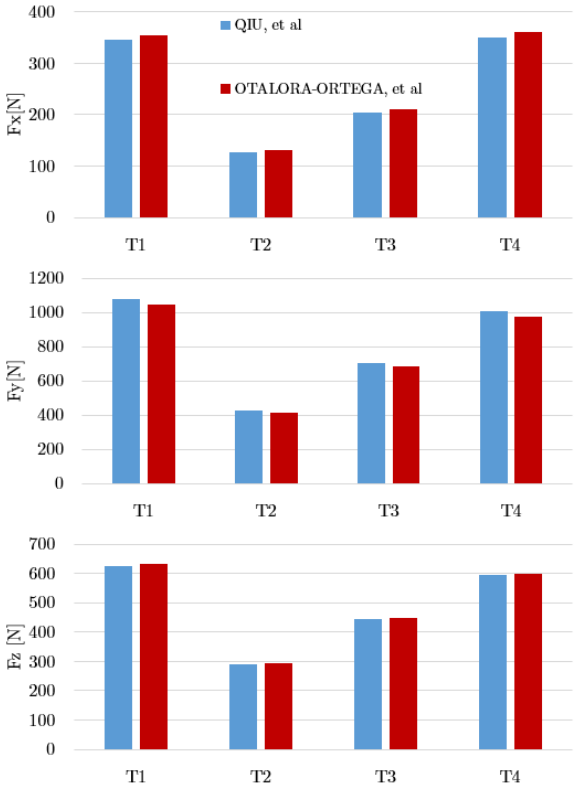

Figure 27: Complete comparison of the cutting forces simulated with the Qiu et al. and the Otalora-Ortega et al. approaches for the experimental plan proposed by Qiu et al [18].

8. Effect of the tool profile geometry and eccentricity

This section aims to simulate a wider scenario to predict the behavior of cutting forces, the uncut chip area evolution, chip volume, and material removal rate (MRR). As the model has been experimentally validated in the previous section, its results are considered representative enough from reality. Until this point, it is evident that the turn-milling operations present an augmented amount of parameters compared with conventional milling. Thus, the simulations are focused on evidence of the effect of varying the tool nose radius and eccentricity, due to these features has been few studied. Table 7 presents the cutting conditions selected to run the simulations.

To focus the attention on the effect of the tool profile and the eccentricity, the rest of the cutting conditions remained constant. As a result of this condition and based on equation 29 reported by

Table 7: Simulation cutting conditions

Rw [mm]	rt [mm]	z [-]	a_p [mm]	V_c $[\frac{m}{min}]$	MRR $[\frac{cm^3}{min}]$
44	16	1	2	400	23.87
Tag	f_z $[\frac{mm}{th}]$	e [mm]	f_a $[\frac{mm}{W_p rev}]$	n_w [rpm]	r_n [mm]
rn4e6	0.2	6	15	3	4
rn4e12	0.2	12	15	3	4
rn4e15	0.2	15	15	3	4
rn5e6	0.2	6	15	3	5
rn4e11	0.2	11	15	3	5
rn4e15	0.2	15	15	3	5
rn6e6	0.2	6	15	3	6
rn6e10	0.2	10	15	3	6
rn6e15	0.2	15	15	3	6
rn8e6	0.2	6	15	3	8
rn8e8	0.2	8	15	3	8
rn8e15	0.2	15	15	3	8

Karaguzel et al. [12], the calculated material removal rate (MRR) is the same for all the simulations. The tool radius selection was based on the search for an actual tool that accepts different geometry inserts. Sandvik R300 mills are indexable round insert mills representing the same tool radius (r_t) for different insert radius (l_s). Hence, the selected tool radius is $r_t = 16\ mm$ and it have tools which accepts inserts of nose radius $r_n = [4, 5, 6, 8]$ mm. Another factor in choosing those tools is that the presented numeric model is versatile, representing diverse tool geometries. However, the specific cutting coefficients are very sensitive to the edge geometry, rake angle, and clearance angle, as shown in figure 21 and equation 28. It is then assumed that the specific force functions do not change if the same mill-inserts family is selected. That is to say that The torus experimental validations are simulated (Sandvik R300), assuming that the edge geometry (circular) rake and clearance angles do not change.

$$MRR = z n_t f_z a_p a_e \tag{29}$$

The selection of the eccentricity levels (e) in the simulations is based on its "optimum" value recurrent in the literature. According to Zhu et al. [27], the value of eccentricity affects the maximum axial feed (f_a) that produces a uniform cylindrical surface. In that work, the condition of eccentricity $r_t - l_s$ is stated as a definitive parameter to set the maximum axial feed where l_s is the usable ra-

dial length of the edge. The equation 30 reported by Zhu et al. [27] shows the states of eccentricity selected to run the simulations. The axial feed is constant for all the simulations and is selected to work in all eccentricity cases. The eccentricity values are selected to fulfill the conditions presented in equation 30. In round inserts, l_s coincides with the insert radius, which defines the tool profile see figure 28. Hence, the values of eccentricity lower and higher of $r_t - l_s$ are the same for the simulations (6 & 15 mm) and the condition of $e = r_t - l_s$ is attached to the nose radius (r_n).

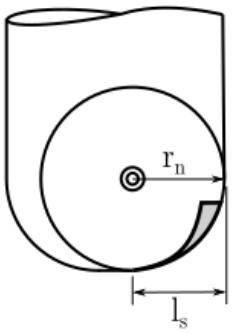

Figure 28: Nose radius and radial usable distance in round inserts mills.

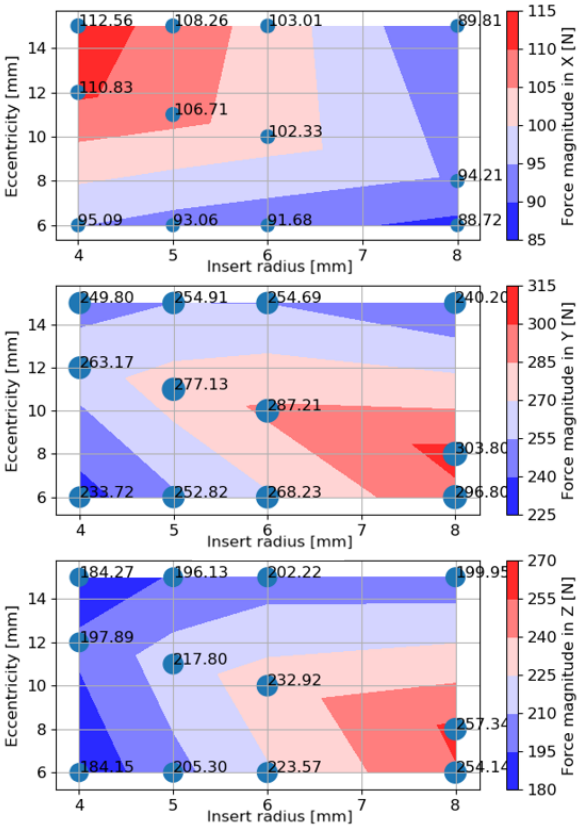

Figure 29: Simulated cutting forces results.

$$
\begin{aligned}
r_t - l_s > e > 0 &\longrightarrow f_{a_{max}} = \sqrt{r_t^2 - e^2} - \sqrt{(r_t - l_s)^2 - e^2} \\
r_t - l_s = e &\longrightarrow f_{a_{max}} = 2\sqrt{2 r_t l_s - l_s^2} \\
r_t > e > r_t - l_s &\longrightarrow f_{a_{max}} = 2\sqrt{r_t^2 - e^2}
\end{aligned}
\tag{30}
$$

Several authors mention this value of eccentricity; nevertheless, there are some controversies due to some of them call it as the "optimum eccentricity" but without theoretical evidence such as Crichigno [9], Karaguzel et al. [12, 28, 25], Zhu et al. [11], Kopač et al. [29], Uysal et al. [30], and Kara et al. [31] among others. However, Karaguzel et al. [30, 32] report increments in the tool life as the eccentricity is augmented; additionally, the maximum life was reported at the condition $e = r_t - l_s$, considered the as its "optimum" value. Although the experimental evidence suggests that this value of eccentricity improves the behavior, it is not rigorous to state "optimum" without the respective theoretical demonstration of the mentioned optimization. Varying the eccentricity in the simulations is intended to show its effect over the uncut chip geometry.

The effect of the nose radius is presented in figure 29 when the graph is analyzed horizontally. The maximum magnitude of the force in the X direction is presented in the upper zone of figure 29. These results show a general trend to decrease when the nose radius increases. This slight decrement obeys to a higher nose radius (r_n) results in a more horizontal tool profile, which aligns the feed and penetration forces with the Z axis. This effect necessarily increments the Z direction forces as presented when the Z force graph is analyzed horizontally. However, the slight force reduction and pronounced increment in $X\&Z$ respectively is also a consequence of the decrement of chip thickness when the nose radius increased. Figure 30 presents the insert radius in scale, and it is possible to see how the chip thickness presents a noticeable reduction even when the depth of cut (a_p) and feed per tooth (f_z) are the same. This thickness reduction corresponds to a higher specific force, as presented in figure 21. It

was then expected that the $Y\&Z$ direction present increments of force as the nose radius (r_n) is also augmenting.

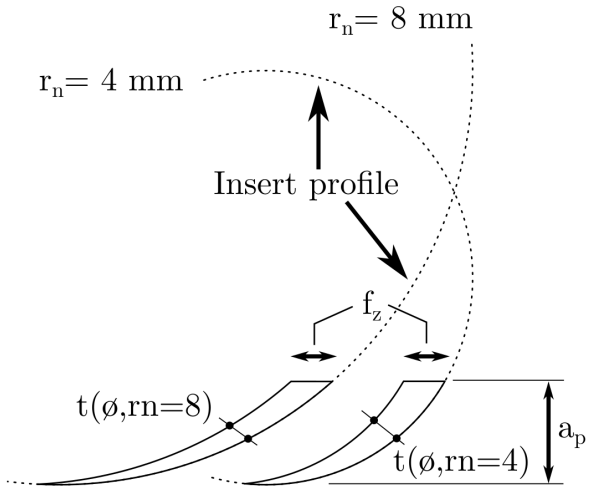

Figure 30: Effect of increasing the nose radius over the chip thickness with the same depth of cut a_p and feed per tooth f_z.

Figure 29 presents the eccentricity effect (e) when the figure is analyzed vertically. Focusing on the X direction, the eccentricity (e) seems to increment the force with the increment of the nose radius (r_n). However, the nose radius ($r_n = 8$) does not follow this trend, due to the maximum force is presented in eccentricity ($e = r_t - l_s$). In the directions ($Y\&Z$) it have been identified maximums of force in the condition ($e = r_t - l_s$) as well, see figure 29 mid and down. The eccentricity (e) modifies the uncut chip geometry that, combined with the workpiece curvature, changes the edge exit angle and the instantaneous depth of cut, presenting the maximum initial instantaneous area scenarios as shown in figure 31. This effect suggests that the chip volume is affected by the eccentricity (e). The area below the curves shown in figure 31 is an indicator of the chip volume changes with the increment of the nose radius (r_n) and eccentricity (e).

Therefore through the model, it is possible to estimate the chip volume presented in figure 32 up. The chip volume presents a considerable change with both variables, the eccentricity (e) and the nose radius (r_n). Even when the cutting conditions for conventional milling are the same for the whole simulations. This condition necessarily means that the material removal rate change, as shown in figure 32 down. These results are found by multiplying

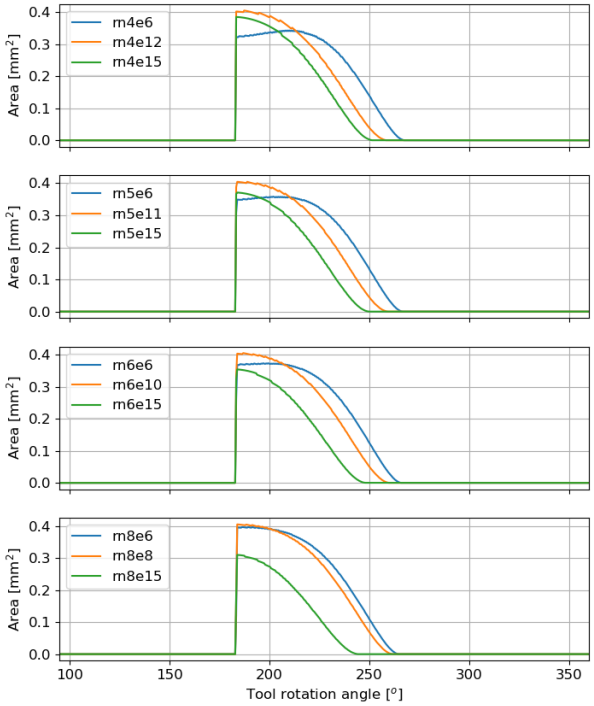

Figure 31: Simulated instantaneous area evolution.

the chip volume by the rotational tool speed (n_t).

None of the estimated MRR presented in the figure 32 coincides with the calculated with the equation 29 reported by Karaguzel et al. [12], thus it is not recommended to use it for turn-milling planning. The volume graph presents a trend to reduce the chip volume if the nose radius (r_n) and the eccentricity (e) is augmented. The decrements in the material removal rate are matched with increments in cutting force due to the modification of the uncut chip geometry. The volume removed by the edge seems to present a maximum local value where the eccentricity (e) is close to 6 mm. Additionally, a smaller insert radius (r_n) shows increments in the removed volume in agreeing with conventional milling, and it coincides with the lowest cutting force prediction. This scenario would be more appropriate than having a low material removal rate and high cutting forces, as shown in the present simulations. The behavior of the cutting forces depends on the uncut chip geometry, and the usable radial length of the edge is an arbitrary parameter. It is possible to find different tools with the same tool radius (r_t) but the different radial usable length of the edge (l_s). Meaning that the "optimum eccentricity" may present diverse values,

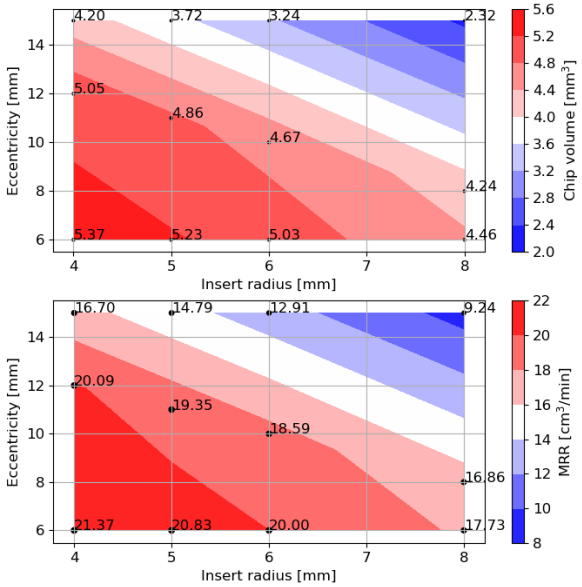

Figure 32: Simulated chip volume results.

but the presented simulations and the experimental results suggest the opposite.

Importantly, the reduction in the material removal rate means that the eccentricity and the tool profile are not removing material that was expected to be. Equation 29 showed a scenario of MRR close to 23 cm^3/min but figure 32 present the minimum value of 9.24 cm^3/min which is a reduction of 61.2%. Consequently, under these conditions, $rn = 8 \& e = 15$, the workpiece might present strong cusp errors due to 61.2% of the mass has not to be removed by the tool. Meaning in reprocesses and loosing of productivity by poor operation planning.

This numerical tool is useful to evaluate diverse machining conditions in a relatively short period. For example, the average time of all of the simulations presented in this research is around 1.5 minutes. It is considering that the discretization process results in 720.000 points, 720 for the angular and 1000 for the radial direction. The variables that affect most the simulating time are the axial feed (f_a) and depth of cut (a_p) because they limit the number of points analyzed in the uncut chip geometry. These short periods contrast with the commercial software that takes several hours to run the calculations facilitating the decision-making on the workshop. The simulating time may vary depending on the number of points of the mesh and the available computational power.

9. Conclusions

This research presented a numerical methodology for studying the effect of the tool profile and the eccentricity in orthogonal turn-milling operations. This machining operation requires several geometrical and kinematic parameters to define the process without including the tool profile geometry selection. Therefore, estimating the operating windows in industrial environments is considerably difficult. Consequently, this research seeks to increase the knowledge related to this machining operation. Thereby the following conclusions raise:

1. The development presented in this research is a powerful tool to simulate vast cutting condition scenarios in a relatively short time. Additionally, it helps to understand that the eccentricity does modify the material removal rate giving a chance to identify geometrical errors by presenting a threaded excess of material in the workpiece result of the insert geometry.

2. The geometric model presented was validated in various stages, such as theoretical and experimental, with two different tool profiles, torus and spherical. Besides, a comparison with Qiu's publication was presented with very close results between the two approaches.

3. Thanks to the versatile approach, the tool profile can be a matter of study; due to, mills profile are in constant innovation, and it is relatively easy to modify it within the model.

4. The simulations performed in **section 8** evidenced the importance of the tool profile in the turn-milling operations performance. This feature could raise scenarios where the tool DOES NOT remove the material uniformly, lying to geometrical errors. These scenarios are feasible if the wrong eccentricity is selected. Even when the eccentricity is under the considerations presented by Zhu et al. [27], these recommendations are only valid for flat end mills.

5. This research did not find theoretical evidence that supports the condition of eccentricity ($e = r_t - l_s$) is "optimum". Indeed, the simulated results showed maximum forces at this condition of eccentricity. This scenario is detrimental to the slender parts, inducing higher dimensional errors, and tool wear.

10. Acknowledgements

The authors hereby thank the project QU4LITY (Grant agreement ID: 825030) and PROCODA (KK-2019/00004) for the financial support to the research work presented in this paper.

References

[1] R. Whalley, M. Ebrahimi, and A. Abdul-Ameer, "Hybrid modelling of machine tool axis drives," *International Journal of Machine Tools and Manufacture*, vol. 45, no. 14, pp. 1560–1576, 2005.

[2] E. Ozturk, L. T. Tunc, and E. Budak, "Investigation of lead and tilt angle effects in 5-axis ball-end milling processes," *International Journal of Machine Tools and Manufacture*, vol. 49, no. 14, pp. 1053–1062, 2009.

[3] M. Wan, H. Yuan, J. Feng, W.-H. Zhang, and W. Yin, "Industry-oriented method for measuring the cutting forces based on the deflections of tool shank," *International Journal of Mechanical Sciences*, vol. 130, pp. 315–323, 2017.

[4] A. d. Lamikiz, L. L. De Lacalle, J. Sanchez, and M. Salgado, "Cutting force estimation in sculptured surface milling," *International Journal of Machine Tools and Manufacture*, vol. 44, no. 14, pp. 1511–1526, 2004.

[5] S. Wang, L. Geng, Y. Zhang, K. Liu, and T. Ng, "Cutting force prediction for five-axis ball-end milling considering cutter vibrations and run-out," *International Journal of Mechanical Sciences*, vol. 96, pp. 206–215, 2015.

[6] S. Wojciechowski and K. Mrozek, "Mechanical and technological aspects of micro ball end milling with various tool inclinations," *International Journal of Mechanical Sciences*, vol. 134, pp. 424–435, 2017.

[7] U. Karaguzel, U. Olgun, E. Uysal, E. Budak, and M. Bakkal, "Increasing tool life in machining of difficult-to-cut materials using nonconventional turning processes," *The International Journal of Advanced Manufacturing Technology*, vol. 77, no. 9-12, pp. 1993–2004, 2015.

[8] K. Orra and S. K. Choudhury, "Mechanistic modelling for predicting cutting forces in machining considering effect of tool nose radius on chip formation and tool wear land," *International Journal of Mechanical Sciences*, vol. 142, pp. 255–268, 2018.

[9] J. M. Crichigno Filho, "Prediction of cutting forces in mill turning through process simulation using a five-axis machining center," *The International Journal of Advanced Manufacturing Technology*, vol. 58, no. 1-4, pp. 71–80, 2012.

[10] A. Calleja, A. Fernández, A. Rodríguez, L. N. L. de Lacalle, and A. Lamikiz, "Turn-milling of blades in turning centres and multitasking machines controlling tool tilt angle," *Proceedings of the Institution of Mechanical Engineers, Part B: Journal of Engineering Manufacture*, vol. 229, no. 8, pp. 1324–1336, 2015.

[11] L. Zhu, H. Li, and C. Liu, "Analytical modeling on 3d chip formation of rotary surface in orthogonal turn-milling," *Archives of Civil and Mechanical Engineering*, vol. 16, no. 4, pp. 590–604, 2016.

[12] U. Karagüzel, E. Uysal, E. Budak, and M. Bakkal, "Analytical modeling of turn-milling process geometry, kinematics and mechanics," *International Journal of Machine Tools and Manufacture*, vol. 91, pp. 24–33, 2015.

[13] J. Shi, Q. Song, Z. Liu, and Y. Wan, "Formulating a numerically low-cost method of a constrained layer damper for vibration suppression in thin-walled component milling and experimental validation," *International Journal of Mechanical Sciences*, vol. 128, pp. 294–311, 2017.

[14] L. Zheng, Y. S. Chiou, and S. Y. Liang, "Three dimensional cutting force analysis in end milling," *International Journal of Mechanical Sciences*, vol. 38, no. 3, pp. 259–269, 1996.

[15] Y. Zhang, S. Li, and K. Zhu, "Generic instantaneous force modeling and comprehensive real engagement identification in micro-milling," *International Journal of Mechanical Sciences*, vol. 176, p. 105504, 2020.

[16] R. Yan, X. Tang, F. Peng, Y. Wang, and F. Qiu, "The effect of variable cutting depth and thickness on milling stability for orthogonal turn-milling," *The International Journal of Advanced Manufacturing Technology*, vol. 82, no. 1-4, pp. 765–777, 2016.

[17] H. Otalora-Ortega, P. Aristimuño, and P. J. Arrazola, "Analytical modeling of the uncut chip geometry to predict cutting forces in orthogonal centric turn-milling operations," *International Journal of Machine Tools and Manufacture*, vol. 144, p. 103428, 2019.

[18] W. Qiu, Q. Liu, and S. Yuan, "Modeling of cutting forces in orthogonal turn-milling with round insert cutters," *The International Journal of Advanced Manufacturing Technology*, vol. 78, no. 5-8, pp. 1211–1222, 2015.

[19] A. Comak and Y. Altintas, "Mechanics of turn-milling operations," *International Journal of Machine Tools and Manufacture*, vol. 121, pp. 2–9, 2017.

[20] H. Schulz and G. Spur, "High speed turn-milling—a new precision manufacturing technology for the machining of rotationally symmetrical workpieces," *CIRP Annals-Manufacturing Technology*, vol. 39, no. 1, pp. 107–109, 1990.

[21] H. Schulz and T. Kneisel, "Turn-milling of hardened steel-an alternative to turning," *CIRP Annals-Manufacturing Technology*, vol. 43, no. 1, pp. 93–96, 1994.

[22] V. Savas and C. Ozay, "Analysis of the surface roughness of tangential turn-milling for machining with end milling cutter," *Journal of Materials Processing Technology*, vol. 186, no. 1-3, pp. 279–283, 2007.

[23] C. Döbberthin, B. Karpuschewski, K. Risse, and L. Deters, "Analysis of the textured surface of tangential turn-milling," *Materials Performance and Characterization*, vol. 6, no. 2, pp. 182–194, 2017.

[24] P. Aristimuño, X. Lazcano, A. Sela, R. Basagoiti, and P. J. Arrazola, "An optimization methodology for material databases to improve cutting force predictions when milling martensitic stainless steel jethete-m152," *Procedia CIRP*, vol. 77, pp. 287–290, 2018.

[25] U. Karagüzel, E. Uysal, E. Budak, and M. Bakkal, "Modelling of turn milling processes for increased productivity," in *The 16 th International Conference on Machine Design and Production*, 2014.

[26] "Webplotdigitizer - copyright 2010-2020 ankit rohatgi," 2020.

[27] L. Zhu, Z. Jiang, J. Shi, and C. Jin, "An overview of turn-milling technology," *The International Journal of*

Advanced Manufacturing Technology, vol. 81, no. 1-4, pp. 493–505, 2015.

[28] U. Karaguzel, M. Bakkal, and E. Budak, "Mechanical and thermal modeling of orthogonal turn-milling operation," *Procedia CIRP*, vol. 58, pp. 287–292, 2017.

[29] J. Kopač and M. Pogačnik, "Theory and practice of achieving quality surface in turn milling," *International Journal of Machine Tools and Manufacture*, vol. 37, no. 5, pp. 709–715, 1997.

[30] E. Uysal, U. Karaguzel, E. Budak, and M. Bakkal, "Investigating eccentricity effects in turn-milling operations," *Procedia CIRP*, vol. 14, no. 14, pp. 176–181, 2014.

[31] M. E. Kara and E. Budak, "Optimization of turn-milling processes," *Procedia CIRP*, vol. 33, pp. 476–483, 2015.

[32] U. Karaguzel, E. Uysal, E. Budak, and M. Bakkal, "Effects of tool axis offset in turn-milling process," *Journal of Materials Processing Technology*, vol. 231, pp. 239–247, 2016.